Spectral flow of a localized mode in elastic media

Marco Miniaci[®], ^{1,*} Florian Allein[®], ¹ and Raj Kumar Pal²

¹Université Lille, CNRS, Centrale Lille, Junia, Université Polytechnique Hauts-de-France, UMR 8520—IEMN—Institut d'Electronique de Microélectronique et de Nanotechnologie, Lille F-59000, France Department of Mechanical and Nuclear Engineering, Kansas State University, Manhattan, Kansas, USA



(Received 11 October 2022; revised 12 October 2023; accepted 16 October 2023; published 11 December 2023)

The introduction of structural defects in otherwise periodic media is well known to grant space control and localization of waves in several fields of physics, from electromagnetism to acoustics and elasticity. Despite the variety of designs proposed so far to achieve mode localization, most of the approaches derive from contextual modifications that do not translate into a design paradigm due to the lack of a general theory. Few exceptions include designs endowed with topological dispersion bands, which, however, require changes over substantial portions of the structure. To overcome these limitations, here we introduce a rationale inspired by fractional electronic charges, to achieve topologically protected localized modes in continuous elastic media. We theoretically predict and experimentally observe the spectral flow of a localized mode across a bulk frequency gap by modulating a single structural parameter at any chosen location of architectured elastic media. The simplicity and generality of this approach may open avenues in designing elastic-wave-based devices for energy localization and harvesting.

DOI: 10.1103/PhysRevApplied.20.064018

I. INTRODUCTION

The quest for media capable of wave localization has attracted increasing interest in many research fields, owing to its promise of fostering new functionalities, such as defect-immune and scattering-free wave propagation [1, 2], object cloaking [3], unidirectional transmission [4,5], and enhanced energy transport and harvesting [6,7], to cite a few. For this reason, wave localization has been extensively studied for over a century in various physical domains, including electromagnetism, elasticity, and acoustics [8,9].

Localized modes can be classified through the symmetry of the structure hosting the wave propagation, i.e., (i) random or disordered [10–14], (ii) quasiperiodic [15–18], and (iii) periodic media with defects [19-22]. In this context, continuous elastic media offer a rich playground in such a quest because of their fourth-order tensor-based physics coupling longitudinal, shear, and flexural deformations [23]. It has been shown that mode localization

Published by the American Physical Society under the terms of the Creative Commons Attribution 4.0 International license. Further distribution of this work must maintain attribution to the author(s) and the published article's title, journal citation, and DOI.

in elasticity emerges by breaking specific symmetries, adding/removing inclusions in the unit cell, or varying its size/shape to create point [24-27] or line defects [28-30]. However, despite the variety of designs proposed so far, most of these approaches are based on ad hoc modifications that do not translate into a general design paradigm allowing a systematic prediction, a priori, of the presence or absence of a localized mode under a geometrical or structural modification. Also, these approaches are extremely sensitive to the presence of additional defects in the structure, implying the risk of uncontrolled frequency shifts of the modes.

The recent introduction of topological protection in elasticity [31-34] has opened new possibilities for a more systematic design procedure to achieve localized modes insensitive to defects [35-39]. Such a robustness arises from dispersion bands with non trivial topology. However, solutions explored so far require material or geometrical modifications over the entire or substantial portions of the structure [40], since such modes arise at the interface between two domains with distinct topological properties characterized by different topological invariants, such as the Zak phase or Chern number [41]. Notable exceptions include fragile topological phases [42,43], where a family of localized modes arise across an interface under twisted boundary conditions [44], and fractional topological charges [45], granting mode localization at the corners of lattice structures.

^{*}marco.miniaci@gmail.com and marco.miniaci@univ-lille.fr

These observations are limited to pressure acoustic waves [43,46] (where the propagation is described through a scalar field potential), electronic charges localizing at corners and dislocation cores due to filing anomalyinduced topological effects [47], and photonic lattices [48]. On the contrary, the spectral flow of localized modes in continuous elastic media has remained elusive so far, due to the unique tensor-based nature of its wave equations [23], implying high modal density and tendency to hybridize under structural modifications. This has often restricted the research of localized modes in solid mechanics to one-dimensional (1D) structures, including one-dimensional soft periodic plates [49], granular crystals [50], and array systems with inerters [51] or resonators [52]. In addition, as nontrivial localized modes are concerned, the current state of the art is limited to modes arising (i) at the edges of 1D chains with specific boundary conditions, (ii) when at least two (different) subdomains are considered, or (iii) when distributed modifications over the structure are introduced.

In contrast to prior works, we propose here an approach to localize a mode within a continuous elastic system at any arbitrary location and by only modifying a single structural parameter (the stiffness) in one unit cell, leaving the remaining structure unaltered.

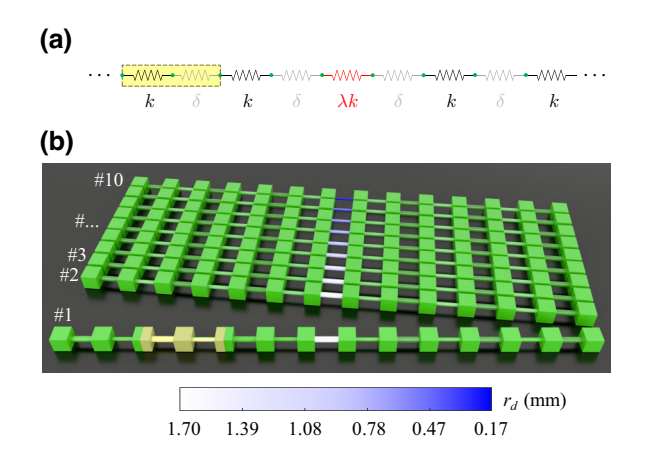
The paper is organized as follows. First, we report the experimental observation of a family of localized modes spanning a frequency band gap between two bulk dispersion bands in polymeric 3D-printed mass-spring systems

that accommodate a smooth local modulation of the stiffness of a single unit cell. Second, the generality of the above rationale is numerically confirmed in the case of platelike structures, i.e., continuous elastic media with 2D in-plane periodicity. In both cases, the observed behavior is accompanied by a thorough interpretation based on a theoretical model allowing us to fully predict, a priori, the presence, or absence, of the localized mode as a function of the structural parameter change. We point out that this approach allows the center of the localized mode to be arbitrarily chosen or located within the original structure, suppressing the need for substantial modifications of the periodic structure, as required, instead, by the traditional topological protection approaches. Furthermore, the procedure, solely involving topological arguments (missing in prior works) remains valid across material properties and length scales, as demonstrated by its extension to higher spatial dimensions (2D hexagonal lattice). We believe that our results may open avenues in designing wave-based devices for elastic energy localization, control, and harvesting.

II. MODAL SPECTRAL FLOW THROUGH STIFFNESS MODULATION (1D CASE)

A. Experimental observation

Figure 1(a) reports a discrete schematic representation of a family of 3D-printed structures, employed to confirm the above rationale. The rectangle shaded in light



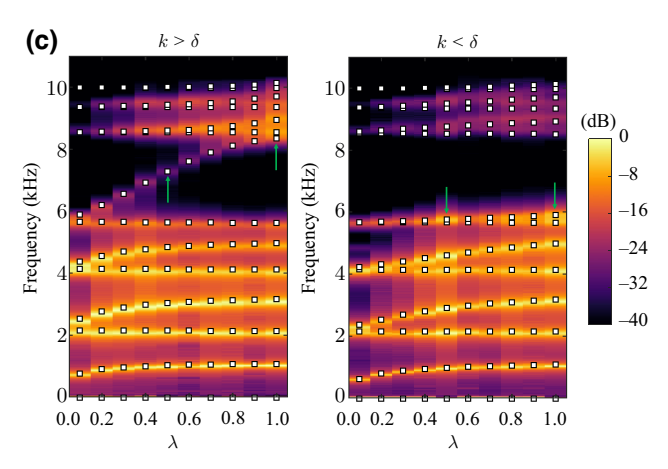


FIG. 1. Observation of the spectral flow. (a) Schematic representation of a mono-dimensional mass-spring chain. The unit cell, highlighted as a light yellow rectangle, comprises two masses (green dots) and two springs of stiffness k (in black) and δ (in gray), respectively. A defect spring (in red) located in the chain is characterized by a stiffness modulated through parameter λ . (b) Three-dimensional rendering of the experimental samples (for $k > \delta$). The stiffness modulation is obtained by gradually varying the radius r_d of the central beam (grading colors going from white to dark blue) connecting its two adjacent masses. Ten stiffness modulations indicated as #1-#10 are considered. (c) Measured frequency response functions (color map) in the 0-11-kHz frequency range for the two classes of elastic chains ($k > \delta$, left panel, and $k < \delta$, right panel) for different values of λ . In the first case, a spectral flow of the eighth mode from the lower to the upper bulk band is observed. In the second case, no crossing is observed. The data at each λ have been individually normalized with respect to their maximum value. Overlaid square white dots indicate analytically calculated eigenmodes. Green arrows indicate the mode shapes that are fully reconstructed and presented in Fig. 3 below.

yellow represents the unit cell of the chain consisting of two identical masses (green dots) and two springs of alternating stiffness k (in black) and δ (in gray), respectively. A defect spring (in red) located in the interior (middle) of the chain is characterized by a stiffness modulation parameter $\lambda \in [0, 1]$.

Figure 1(b) reports a 3D rendering of the printed structures manufactured to realize the elastic analogue of the above-described discrete system. The unit cell (in yellow) can be divided into three regions: a thick one with square cross section, corresponding to the masses of the discrete chain (masses in what follows) and two thin beams with circular cross section of different radii, corresponding to the springs of stiffness k and δ (springs in what follows). The axial stiffness of each beam is EA/L to first order, with E, A, and L the material Young modulus, the cross-section area, and the length of the beam, respectively (geometrical and material parameters of the considered unit cell are reported below).

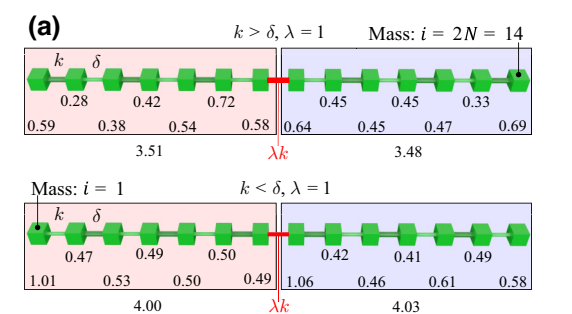
The first step towards a clear observation of a topologically protected modal spectral flow is to realize a complete band gap for all the possible elastic polarizations (bending, shear, torsional, and axial modes) of the considered unit cell. This is done by choosing an appropriate set of geometric parameters for the unit cell under investigation (considered as infinitely repeated along the x direction), when $k \neq \delta$. In our case, a band gap between 5840 and 8280 Hz is opened when $k = 2\delta$ (see Appendix A for details on the dispersion diagram and mode shapes, and the geometrical and material parameters of the considered unit cell). As the second step, a modulation of one of the stiffer springs (those characterized by rigidity k) is introduced at an arbitrary location (chosen for simplicity at the center of the chain in our case) within a finite structure, and thus now made of a finite number of unit cells (seven in our case) to induce a selective shift in the natural frequencies of the eigenmode closest to the band gap.

To this end, two classes of finite chains hosting 14 masses (see Appendix B) are fabricated through additive manufacturing (Stratasys Objet350 Connex3) using the thermoplastic polymer VEROTM with the following nominal properties: density $\rho = 1180 \text{ kg/m}^3$, Young's modulus E = 2.96 GPa, and Poisson ratio $\nu = 0.38$. The geometrical parameters of the unit cells are the following: (i) side of the square mass a = 10 mm, (ii) length of the beams L = 15 mm, (iii) radii of the beams corresponding to the springs of stiffness k and δ in the discrete case are $r_1 = 1.20 \text{ mm}$ (k) and $r_2 = 1.20 \times \sqrt{2} \simeq 1.70$ mm (δ) for the case $k < \delta$ and $r_1 = 1.20 \times \sqrt{2} \simeq 1.70$ mm (k) and $r_2 = 1.20$ mm (δ) for the case $k > \delta$. In both cases, the radius of the defect is set to $r_d = r_2 \sqrt{\lambda}$. Ten stiffness modulations are introduced through a gradual variation of radius r_d of the central beam of the finite chain [grading colors shading from white to dark blue in Fig. 1(b)] indicated as λk , with $\lambda \in [0.1, 1]$, and enumerated as #1–#10, corresponding to $\lambda = 1$ and $\lambda = 0.1$, respectively. A photograph of the manufactured samples is reported in Appendix B.

Two distinct cases are considered to distinguish between a trivial stiffness alteration and a topological one leading to a modal spectral flow: (i) $k > \delta$ and (ii) $k < \delta$. The transmissibility of the two classes of structures is investigated by scanning laser doppler vibrometry (SLDV) of the samples. Longitudinal waves are excited into the specimens by imparting axial displacements and longitudinal velocity is acquired (Appendix C reports the details of the experimental configurations). The transmissibility is calculated as the ratio of the velocity amplitude detected at the scanning points and at the excitation points. Figure 1(c) reports the frequency response function in the 0–11kHz frequency range for the two cases $(k > \delta)$, left panel, and $k < \delta$, right panel) when ten different values of λ are adopted. In the first case, a spectral flow of the eighth mode from the lower to the upper bulk region is observed as energy spots passing across the entire band gap when λ is varied in the [0.1, 1] range. On the contrary, when $k < \delta$, no crossing is observed as λ is changed. This provides a direct observation of the modal spectral flow. The experimental results are in perfect agreement with the natural frequencies of the axial modes of the specimens calculated analytically by solving the corresponding eigenvalue problem (see Appendix D for details on the analytical calculations) and reported as overlaid white squares. The rigid longitudinal translation modes at zero frequency are filtered out in the experimental measurements through a high-pass band filter. An additional comparison between the analytical results and further numerical calculations are also provided in Appendix E.

B. Integrated mode density

The emergence (or absence) of the localized modes derives from topological properties associated with the defectless periodic structure. To reveal the nontrivial origin of the mode spanning the whole band gap, the integrated mode density (IMD) is determined from the experimental frequency responses of the finite periodic structure without defect, i.e., when $\lambda = 1$ [see Fig. 2(a)]. The red segment identifies, for each structure under consideration ($k > \delta$ in the top panel and $k < \delta$ in the bottom panel), the interface dividing the system into two subdomains (at the left and at the right of the red springs of rigidity λk) hosting S =7 masses or 2N - S = 14 - 7 = 7 masses, respectively (2N = 14) is the total number of masses in the considered finite structures, where N is the number of unit cells composing the finite structure). IMD is calculated by considering the subdomain on one side of the interface (either the left one or the right one) having S, or 14 - S, masses



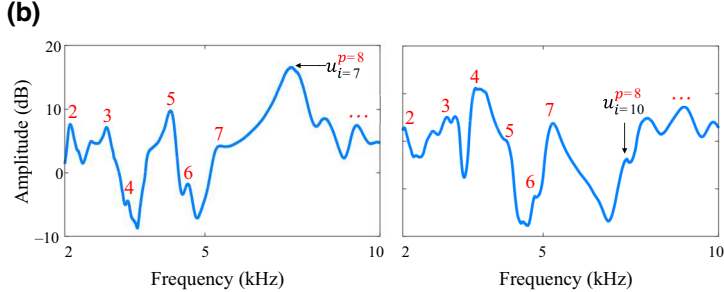


FIG. 2. Integrated mode density: the signature of the nontrivial topological behavior of the spectral flow. (a) Three-dimensional rendering of the examined structures when $k > \delta$, $\lambda = 1$ (top panel) and $k < \delta$, $\lambda = 1$ (bottom panel). The location where the defect is introduced as λ is varied (red segment) divides the domain into two subdomains. The values of the experimentally determined integrated mode density (IMD) for the domains on each side of the interface are reported in the light pink and light purple rectangles, respectively. The IMD is a fraction when $k > \delta$ and an integer when $k < \delta$, unequivocally confirming the nontrivial and trivial topologies of the two classes of structures, respectively. The numbers near each mass indicate the contributions to the IMD, $\sum_{p=1}^{Q} u_{ip}^2$. (b) Frequency content of the measured axial displacement u_i of masses i=7 (left panel) and i=10 (right panel). The red numbers highlight the peaks corresponding to the mode shapes of the eigenfrequencies below the band gap in the left panel of Fig. 1(c). The y axis of the figures, expressed in decibels, derives from $20 \log_{10} u$, where u is the longitudinal displacement derived from the SLDV acquisitions at the edge of the sample.

and the Q mode shapes corresponding to the eigenfrequencies below the band gap (Q=7 in our case). The presence or absence of localized modes is determined by

$$IMD = \sum_{p=1}^{Q} \sum_{i=1}^{S} u_{ip}^{2} = \begin{cases} \text{integer,} & \text{no localized mode,} \\ \text{fraction,} & \text{localized mode,} \end{cases}$$
(1)

with u_{ip} the measured axial displacement of each mass. Each mode shape p is normalized as $\sum_{i=1}^{N} u_{ip}^2 = 1$. A fractional (integer) value of the IMD guarantees the presence (absence) of localized modes under the considered structural modification at the chosen location, in analogy to the fractional charges in electronic media [48]. To determine the IMD, the axial displacement u_{ip} corresponding to each mass $i \in [1, 2N = 14]$ of the $\lambda = 1$ chain for all the mode shapes below the band gap are extracted from the measured frequency response functions, as those reported in Fig. 2(a) for i = 7 and 10. In these plots, the red numbers highlight the peaks corresponding to the mode shapes of the left panel of Fig. 1(c) $(k > \delta)$ and $(k > \delta)$ and $(k > \delta)$. The bold numbers below the structures in Fig. 2(a) show that the IMD is a fraction (3.5) when $k > \delta$ and an integer (4) when $k < \delta$, confirming the appearance of a localized mode at the interface under structural modification [48] in the first case. This confirms the nontrivial (trivial) topology of the $k > \delta$ $(k < \delta)$ structure [47], with the topology being protected by the periodicity of the structure along the axial direction. The numbers near each mass in the light pink and light purple rectangles indicate their respective contributions to the IMD, $\sum_{p=1}^{Q} u_{ip}^2$.

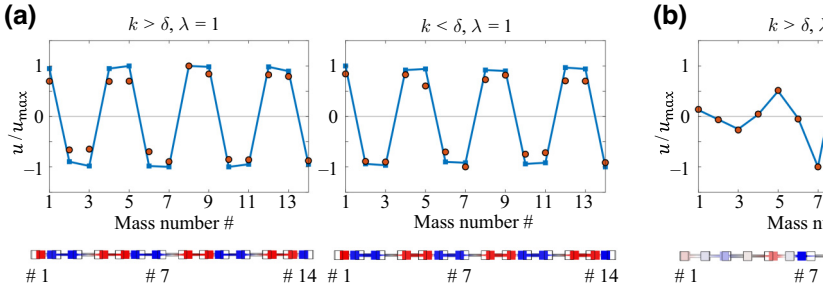
C. Eigenvector reconstruction

When $k > \delta$, a family of modes, whose natural frequencies traverse the band gap as the radius of a single beam is varied, exists. To verify that these modes are indeed localized (contrary to the case of $k < \delta$), the eighth mode shape is reconstructed (in terms of amplitude and phase) for the two classes of structure.

Figure 3(a) reports the normalized amplitudes of the displacement of the masses for the eighth mode shape of the two chains ($k > \delta$, left panel, and $k < \delta$, right panel), setting λ to 1 [green arrows in Fig. 1(c)]. Measured values (red dots) are superimposed to the analytical predictions (blue lines with square markers). Excellent agreement is found. In both cases the displacement of the masses spans the entire chain, confirming that the deformation can be identified with a Bloch mode lying in the higher and lower bulk bands (see Appendix D), as indicated by the green arrows at $\lambda = 1$ in Fig. 1(c), pointing up or down, respectively.

Figure 3(b) reports the normalized amplitudes of the displacement of the masses for the eighth mode shape of the two chains ($k > \delta$, left panel, and $k < \delta$, right panel), now setting λ to 0.5. The chain with $k > \delta$ (left panel) presents a mode shape localized at the center of the structure (in correspondence of the stiffness modulation), with its displacement magnitude rapidly dropping in the peripheral masses. On the contrary, when $k < \delta$ (right panel), the eighth mode shape, still belonging to the (lower) bulk band, shows no localization. Its displacement is maximum at the sample boundaries and is characterized by a slight amplitude decrease at the center of the structure.

The experimental results are corroborated by numerical finite-element models; we report the deformation of the



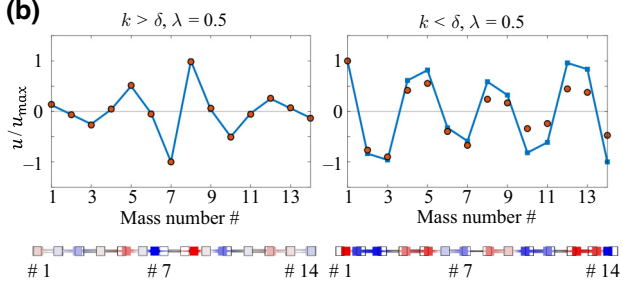


FIG. 3. Eigenvector reconstruction. Measured normalized amplitudes (red dots) versus analytical predictions (blue lines with square markers) of the axial displacement of masses for the eighth mode shape of the two chains $(k > \delta)$, left panels, and $k < \delta$, right panels), setting parameter λ to (a) 1 and (b) 0.5, respectively. When $\lambda = 1$, the displacement of the masses spans the entire chain regardless of $k > \delta$ or $k < \delta$. When $\lambda = 0.5$, if $k > \delta$, a mode shape localized at the center of the structure is observed, whereas no localization occurs when $k < \delta$. The amplitudes of both the measured and calculated mode shapes have been normalized to the absolute value of the maximum displacement (measured or calculated, respectively). The insets below each subfigure show the displacement of the masses (derived from finite-element models) with respect to their equilibrium position (the reference system is set at the center of the chain).

mode shapes below each subfigure. Some of the masses are numbered for reference. The axial displacement of the masses with respect to their equilibrium position is reported. The displacement is normalized with respect to the absolute value of the maximum axial displacement. Additional details of the numerical models are reported in Appendix F.

D. Rationale

To understand the rationale of the observed spectral flow as λ is varied in the $k > \delta$ chain, two discrete chains in the form of rings are considered [Fig. 4(a)]. Depending on where the stiffness modulation is applied, i.e., on the spring of stiffness k or δ (highlighted in red), two conditions are possible: (i) if $\lambda = 1$, both chains in Fig. 4(a) reduce to the closed one reported in the central panel of Fig. 4(b); (ii) when $\lambda = 0$, the chains in Fig. 4(a) may result in the two open chains in the top and bottom panels of Fig. 4(b), depending on whether the k or δ spring is removed, respectively. Two classes of chains can thus be identified: closed (in the form of a ring) and open (one spring is missing).

In both cases (open or closed finite chains), all the natural frequencies lie in bulk bands [light blue rectangles in Figs. 4(d) and 4(e)]. Counting their number leads to different values for the different chain configurations. This difference is the key factor determining the observed spectral flow. Indeed, when the limit condition of $\lambda = \delta = 0$ is enforced, the chains become disjoint units of masses and springs [Fig. 4(c)]. Each connected mass-spring subsystem generates eigenmodes with natural frequencies assuming 0 or $\sqrt{2k/m}$ values. Counting the number of such disjointed mass pairs gives the corresponding multiplicities of natural frequencies in these limit-case systems. For example, the open ring in the bottom panel of Fig. 4(c) has N multiples of $\omega = 0$ frequencies when $\lambda = \delta = 0$, where N is the number of unit cells. On the contrary, the open chain

in the top panel of Fig. 4(c) has N+1 multiples of $\omega=0$ frequencies and N-1 multiples of $\sqrt{2k/m}$ frequencies, since, going to the limit of $\lambda=\delta=0$, two masses are left unconnected. Since all the natural frequencies lie in the dispersion bulk bands that do not touch when $k>\delta$, the number of eigenmodes in each band is also expected to remain unaltered for all the family of possible chains with decreasing δ (up to the limit condition of $\lambda=0$).

If λ is varied from 0 to 1, both (open) chains shown in the top and bottom panels of Fig. 4(b) reduce to the closed one reported in its middle panel. In the first case, the number of modes in the lower band must change from N+1 to N as we transition from the open to the closed chain. Since the eigenvalues of the stiffness operator and thus natural frequencies of the chains vary smoothly with parameter λ , the only way to achieve this change in the number of modes is to have a net spectral flow of one mode from the lower to the upper bulk band [Fig. 4(d)]. On the other hand, for the case of spring stiffness changing by $\lambda\delta$, the number of modes remains the same in each band and no net spectral flow will happen as λ varies from 0 to 1 [Fig. 4(e)]. The spectral flow-based arguments described above guarantee the emergence of a nontrivial mode spanning the whole band gap when $\lambda \in [0, 1]$. If $\lambda > 1$ (and $k > \delta$), a localized mode may still appear in the band gap, depending on the relative values of k and δ . However, this mode is trivial in the sense that it is guaranteed not to span the band gap as parameter λ is varied (see Appendix D).

III. SPECTRAL FLOW IN THE CASE OF 2D PERIODICITY

A. Numerical observation

The generality of the above-described rationale is here further confirmed by considering platelike structures, i.e.,

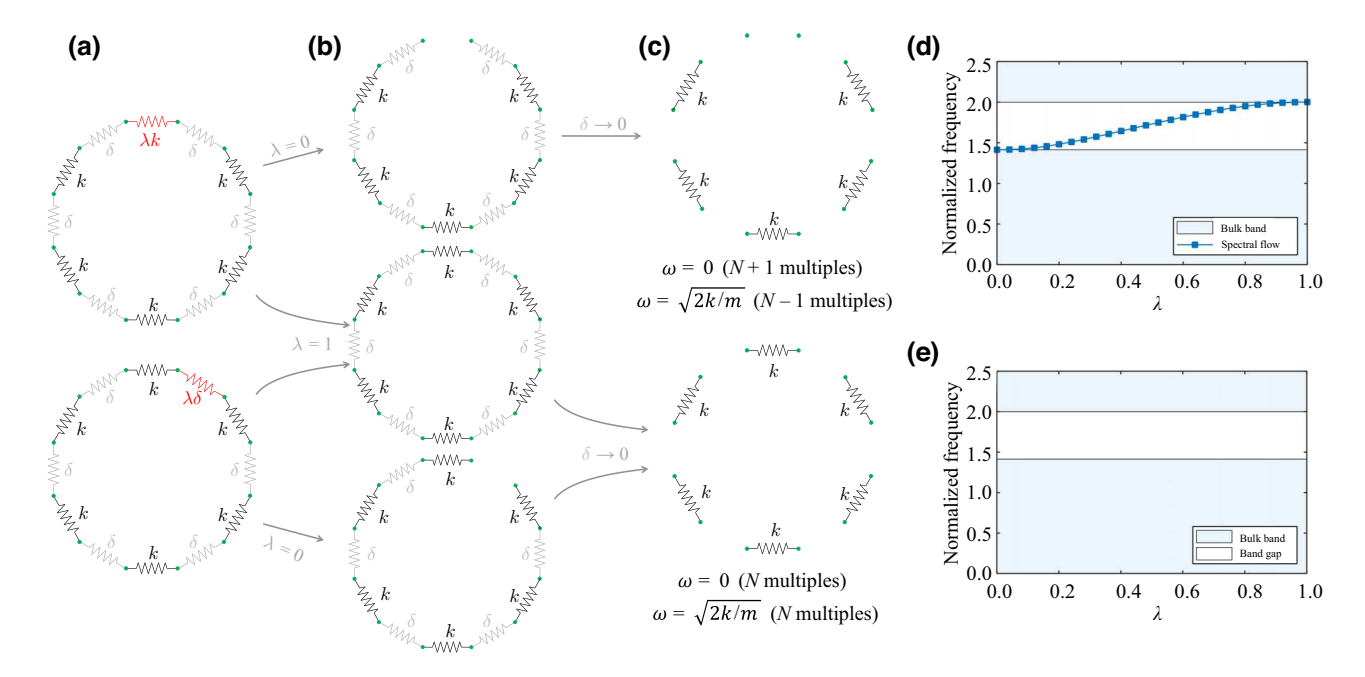


FIG. 4. Theoretical framework. (a) Schematic representation of two 1D mass-spring chains arranged in the form of rings. The modulation parameter λ is applied to the spring of stiffness k or δ (highlighted in red) in the top and bottom panels, respectively. (b) If $\lambda = 1$, the two chains both reduce to a close ring (central panel). If $\lambda = 0$, two different open chains are obtained depending on if the spring of stiffness k or δ is removed—top and bottom panels, respectively. In both cases, the natural frequencies of the chains entirely lie in the bulk bands—light blue rectangles in subfigures (d) and (e). Taking the lower spring stiffness δ to 0 (we recall here that $k > \delta$) as a limiting process ($\delta \to 0$), two different sets of disjoint chains are obtained—top and bottom panels of subfigure (c). These systems are characterized by a couple of natural frequencies ω with multiplicity N + 1/N - 1 or N, respectively. In the first case, a variation of λ from 0 to 1 brings a transition from an open to a closed chain; thus, the number of modes on the lower bulk band changes from N + 1 (when $\lambda = 0$) to N (when $\lambda = 1$). (d) Since the eigenvalues of the stiffness operator, and thus the natural frequencies of the chains, vary smoothly with parameter λ , the only way to achieve such a change in the number of modes is to have a net spectral flow of one mode from the lower to the upper bulk bands. (e) When the spring stiffness δ is changed through parameter λ , the number of modes remains the same on each band (N); thus, there is no net spectral flow. Although the rationale is here demonstrated via Su-Schrieffer-Heeger (SSH) model-based considerations (due to its simplicity), we point out that this approach also applies to higher-dimensional structures (see the case of the hexagonal lattice reported in Sec. III below).

elastic media with 2D in-plane periodicity. The design of the unit cell hosting the spectral flow of a family of localized modes is driven by a lumped discrete model (made of masses and springs). The masses of the previous lumped schematics reported in Fig. 4 are now distributed in a hexagonal lattice and, again, connected by springs of different stiffness k and δ , as shown in Fig. 5(a). The parallelogram shaded in light yellow represents the unit cell of the lattice. It consists of two masses (green dots) and of springs of stiffness k (in black) and δ (in gray). The masses are identical, and exhibit only one degree of freedom: the out-of-plane motion. The structure has C_{2v} (twofold rotation and reflection) symmetry and a band gap opens when $k > 2\delta$ (see the discrete model reported in Appendix G).

Also in this case, the effect of a defect spring [high-lighted in red in Fig. 5(a)] characterized by a stiffness modulation parameter λ and located anywhere in the structure (either on the beam of softer δ or stiffer k rigidity) is examined to determine if it leads to a topologically protected localized mode.

The corresponding continuous elastic medium realizing the analogue of the above-described discrete unit cell is reported in Fig. 5(b). It consists of an x-like unit cell, comprising a hexagonal lattice when repeated along the two lattice directions. It is made of aluminium and it is decorated on both sides with periodic steel pillars at the vertices of the hexagonal lattice. The geometrical parameters of the unit cell are $L_1 = \alpha a/\sqrt{3}$, $L_2 = 0.5\sqrt{L_1^2 + a^2 - \sqrt{3}L_1a}$, h = a/20, H = a/10, and $\phi = a/20$, where a = 1 m is the unit cell lattice parameter and $\alpha = 0.6$ (α indicates the ratio of the length L_1 of the interior beam of the unit cell to the length L^* of the same beam in a corresponding uniform hexagonal lattice—a uniform hexagonal lattice would exhibit $\alpha = 1$; such a 40% reduction has been adopted to assign this beam the desired higher stiffness). The geometrical parameters are chosen so that the beams composing the hexagonal lattice have the same rectangular cross sections, ht, but different lengths, L_1 and $2L_2$. As the flexural stiffness of a beam scales as $t(h/L)^3$, parameters L_1

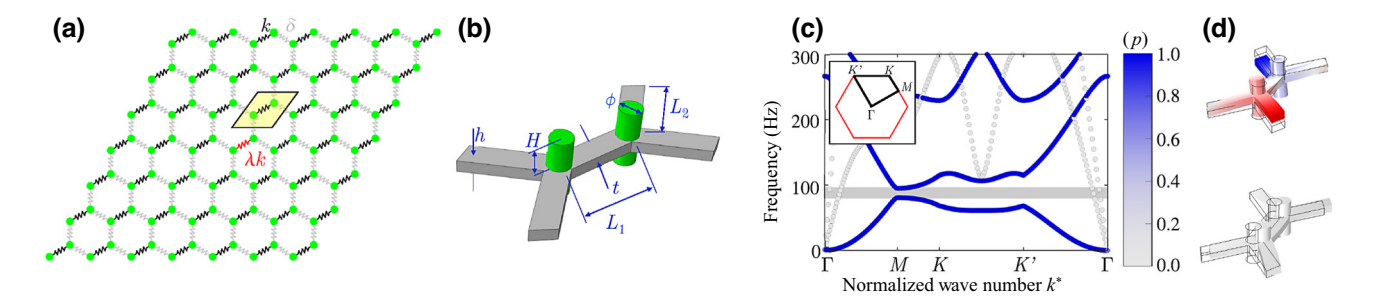


FIG. 5. Case of platelike structures: from the discrete to the continuous model. (a) Schematics of a 2D discrete lattice with in-plane periodicity. The masses can move out of plane only, and are connected by springs of different stiffness k and δ , highlighted in black and gray, respectively. The shaded yellow parallelogram indicates the unit cell. A defect introduced as a spring characterized by a stiffness modulation parameter λ and located anywhere in the structure (highlighted in red) is reported. (b) Unit cell of a continuous elastic medium realizing the analogue of the discrete lattice in (a). It consists of an aluminum hexagonal lattice decorated with steel pillars attached on both sides of the plate. The geometrical parameters are chosen so that the beams composing the hexagonal lattice have the same cross sections, ht, but different lengths, L_1 and $2L_2$. (c) Dispersion curves for the unit cell represented in (b) as infinitely repeated in the plane. The inset shows the Γ -M-K-K' boundary of the irreducible Brillouin zone. The dispersion curves are color coded based on a polarization coefficient p that varies gradually from 0 (light gray; predominantly in-plane modes) to 1 (blue; predominantly out-of-plane modes). The opening of a band gap for flexural waves between 80 and 95 Hz is emphasized by the light gray rectangle. (d) The second and third mode shapes at half of the K-K' path. The colors, indicating the out-of-plane displacement, emphasize the radically different nature of the two modes (out of plane and in plane).

and L_2 allow us to tune the stiffness of the springs so as to obtain an analogy of the different stiffness k and δ provided in Fig. 5(a). The following mechanical parameters (assuming a linear elastic constitutive law) are adopted: $\rho = 2700 \text{ kg/m}^3$, E = 70 GPa, and $\nu = 0.33$ for the aluminium (the beams), and $\rho = 7800 \text{ kg/m}^3$, Young's modulus $E = 100 \text{ kg/m}^3$.

210 GPa, and Poisson ratio $\nu = 0.3$ for the steel (the pillars).

For the sake of simplicity, we focus our attention on flexural waves. Also in this case, the first step to achieve a nontrivial protected spectral flow is to realize a frequency band gap for the wave polarization of interest. In

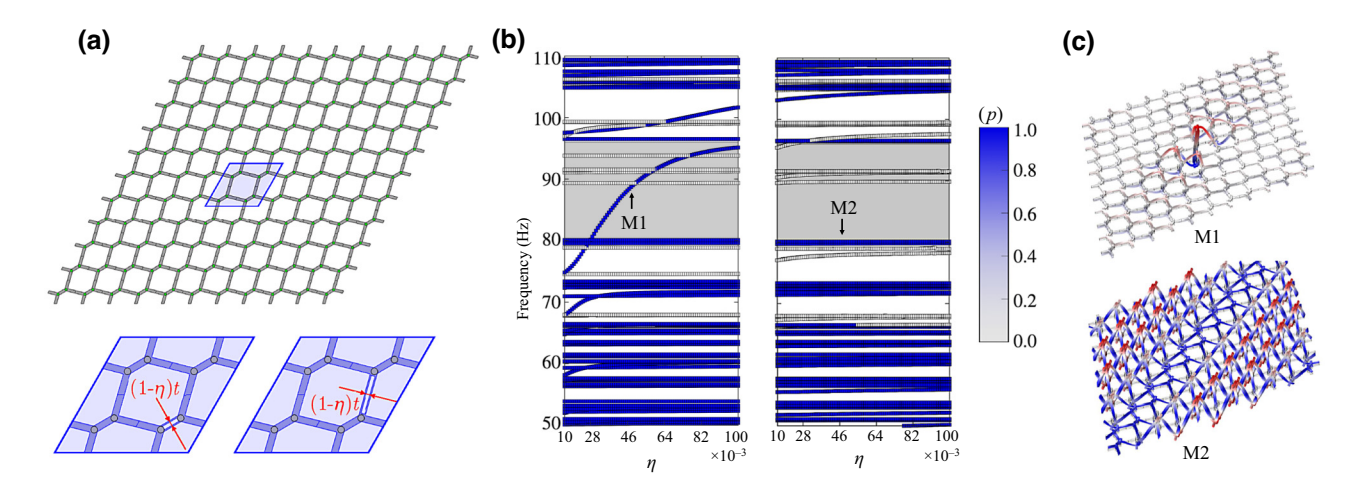


FIG. 6. Spectral flow in the hexagonal lattice. (a) In the top panel a finite structure composed of 11×11 unit cells of the type reported in Fig. 5(b) is presented. The two types of local stiffness modulations achieved by introducing a slit in the shorter or longer beam are reported in the bottom panels. The modulation is achieved through parameter η , which is responsible for the variation of the width of the slit. (b) Eigenfrequencies extracted via finite-element analyses as a function of the modulating parameter η in the 0–110-Hz frequency range for the two cases (ηk and $\eta \delta$). Frequencies are color coded based on coefficient p to distinguish in-plane (gray dots) and out-of-plane (blue dots) modes. In the left panel, a spectral flow across the entire band gap (gray rectangle) is visible when the k spring is varied as ηk with $\eta \in [0.01, 0.1]$. On the contrary, in the right panel, when the δ spring is varied, no band gap crossing happens. (c) The mode shape is localized as it crosses the band gap (top panel), whereas it concerns the entire structure when no spectral flow is observed (bottom panel). In both cases, the mode shape is extracted for $\eta = 0.04$ —black arrows in (b).

other words, we look for a band gap concerning flexural displacements not coupling with other polarizations. The dispersion curves for the unit cell represented in Fig. 5(b) as infinitely repeated in the plane are reported in Fig. 5(c). The dispersion curves are color coded based on a coefficient p that quantifies the mode polarization according to the expression $p = \int_V |w|^2 / \sqrt{u^2 + v^2 + w^2}$ [53], with (u, v) the in-plane components and w the out-of-plane component of the displacement vector. The polarization factor color bar varies gradually from 0 (light gray; predominantly in plane) to 1 (blue; predominantly out of plane). With these metrics, the opening of a band gap for flexural waves between 80 and 95 Hz is clearly visible (emphasized by the light gray rectangle) when k =2δ. The band diagram is calculated by imposing Bloch-Floquet periodic boundary conditions at the boundary faces of the unit cell with normal direction lying in-plane and by varying the wave vector along the Γ -M-K-K' boundary of the first irreducible Brillouin zone [see the black line in the inset reported in Fig. 5(c)]. We point out here that (i) the lattice vectors $(\mathbf{a}_1, \mathbf{a}_2)$ are of equal magnitude and make a 60° angle to each other and that (ii) the reciprocal lattice vectors \mathbf{b}_i satisfy the condition $\mathbf{a}_i \cdot \mathbf{b}_i = 2\pi \delta_{ii}$, and they are also of equal magnitude and at angle $2\pi/3$. Thus, although the beam segments

are of distinct lengths, the first Brillouin zone remains a regular hexagon. Nevertheless, owing to the twofold rotational symmetry of the lattice, the irreducible Brillouin zone is larger than that of a regular hexagonal lattice. Figure 5(d) reports the second and third mode shapes at half of the K-K' path. The colors, indicating the out-of-plane displacement, emphasize the radically different nature of the two modes.

As the second step, a controlled local modulation of a spring of the unit cell is introduced by producing a slit at an arbitrary position within a finite structure of $M \times N = 11 \times 11$ unit cells [see Fig. 6(a)] to induce selective shifts in the natural frequencies of the flexural eigenmode closest to the band gap. Here the width t of a beam segment is varied by a factor η to achieve the stiffness modulation.

As in the previous 1D case, two conditions are considered, namely, when (i) the stiffer spring k is modulated and (ii) the softer spring δ is modulated [see the left and right bottom panels of Fig. 6(a), respectively]. The eigenfrequencies of the two classes of structures are extracted via finite-element analyses and 100 stiffness modulations are considered with $\eta \in [0.01, 0.1]$; see Fig. 6(b). The eigenfrequencies are reported as a function of η in the 0–110-Hz frequency range when the k spring is modulated (left panel) and when the δ spring is modulated (right panel).

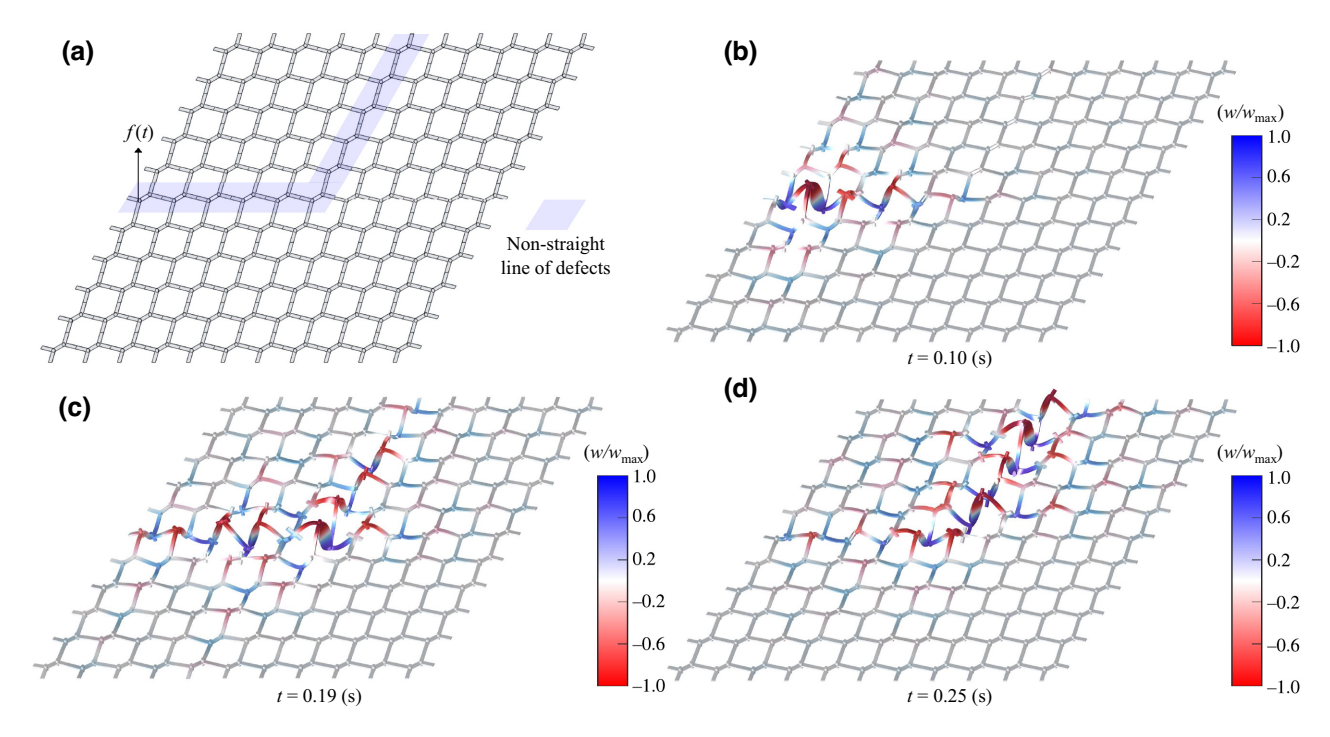


FIG. 7. Transient simulation along a nonstraight line of defects. (a) Finite structure made of 11×11 unit cells of the type reported in Fig. 5(b), hosting a line of defects along an L path (highlighted by the light blue shading). The black arrow indicates the point of excitation, where an out-of-place displacement has been imposed. The excitation signal F(t) consists of a Hanning modulated 21-sine cycle centered at 90 Hz. (b)–(d) Numerical wave-field reconstructions showing how the localized mode propagates rightward, traversing the turn at the middle of the plate. The time snapshots show the out-of-plane displacement before the wave approaches [t=0.1 (s)], traverses [t=0.19 (s)], and passes [t=0.25 (s)] the turn. The colors, varying from blue to red, correspond to the normalized out-of-plane displacement w/w_{max} of the plate.

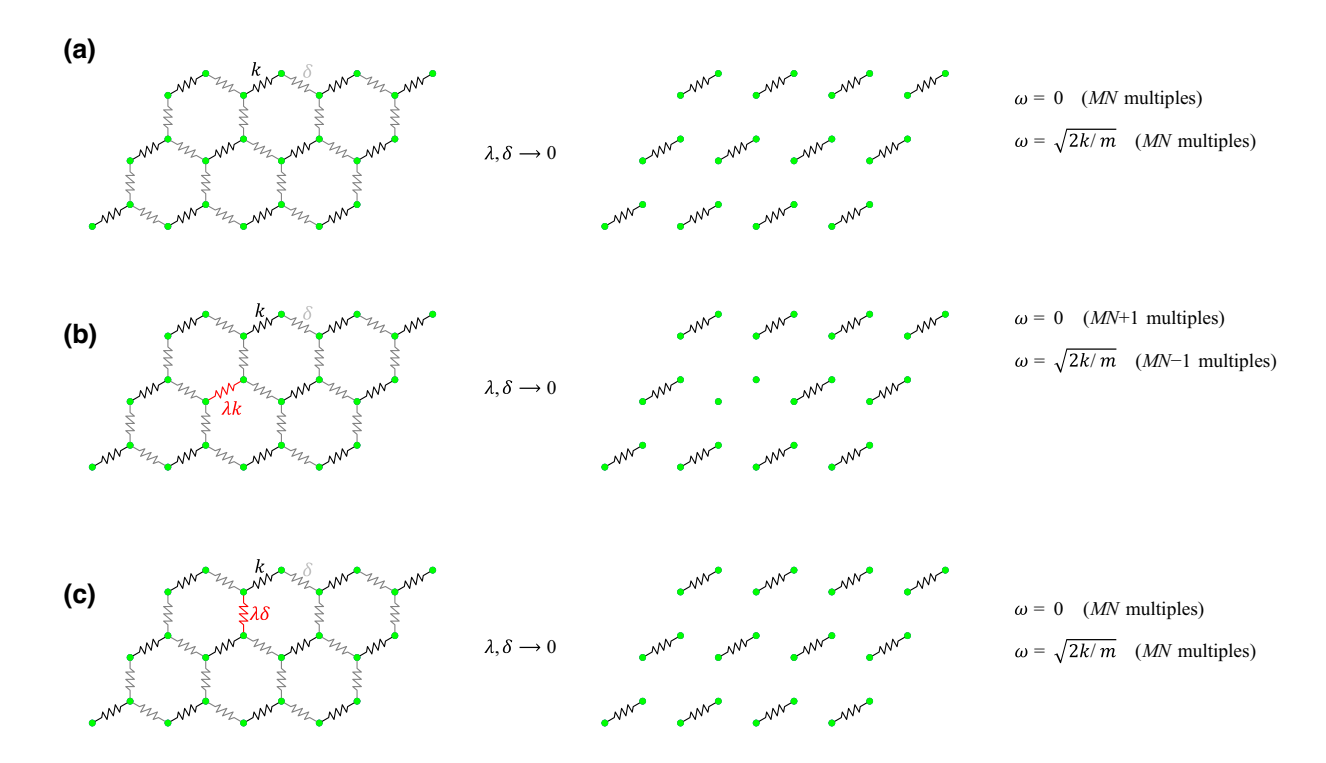


FIG. 8. Extension of the theoretical framework explaining the emergence (absence) of spectral flow in the case of 2D in-plane periodicity. (a) Schematic representation of the 2D mass-spring hexagonal lattice. The modulation parameter λ can be applied to the spring of stiffness k, left panel of (b), or δ , left panel of (c), corresponding to the springs highlighted in red. Taking the lower spring stiffness δ to 0 (we recall here that $k > \delta$) as a limiting process, two different sets of disjoint mass-spring systems are obtained—central panels of (b) and (c). These systems are characterized by a couple of natural frequencies ω with multiplicities MN or MN + 1 and MN - 1, as shown in the right panels of (a)—(c).

Also in this case the frequencies are color-coded based on the previously described coefficient p so that we can distinguish between in-plane polarized and out-of-plane polarized modes. In the first case, a spectral flow across the entire flexural band gap (light gray rectangle) happens when η is varied. On the contrary, when the softer spring (δ) is modulated by the same factor η , no crossing happens.

Finally, to confirm the localized nature of the migrating mode (i.e., when a stiffer spring k has a slit), the mode shapes for the two classes of structures $[\eta k]$ in the top panel of Fig. 6(c) and $\eta \delta$ in the lower panel of Fig. 6(c)] for $\eta = 0.04$ [green arrows in Fig. 6(b)] are reported. From the examination of Fig. 6(c), it is evident that the mode under investigation [green arrows in the left and right panels of Fig. 6(b)] remains localized while migrating from the lower bulk region to the higher one (where the deformation joins a bulk behavior). On the contrary, in the second case [lower panel of Fig. 6(c)] the displacements corresponding to the same mode number span the entire structure, i.e., it is a bulk mode. These computations provide numerical evidence of the aforementioned modal spectral flow in 2D continuous elastic media.

B. Transient simulation along a nonstraight line of defects

To demonstrate the potential of such topological localized modes for wave guiding, we analyze a nonstraight line of defects introduced to the 2D finite structure composed of 11×11 unit cells, as shown in Fig. 7. The nonstraight line of defects, arranged in an L-shaped pattern, is highlighted with light blue shading. Out-of-plane waves are excited at the location indicated by the black arrow. To be sure of injecting into the plate frequencies as close as possible to those of mode M1 shown in Figs. 6(b) and 6(c), we choose the excitation signal F(t) as a Hanning modulated 21-sine cycle centered at 90 Hz.

Figures 7(b)–7(d) present the numerical wave-field reconstructions of the localized mode propagating rightward and traversing the turn at the middle of the plate. The time snapshots are taken when the wave approaches [t=0.1 (s)], traverses [t=0.19 (s)], and passes [t=0.25 (s)] the turn. The colors, varying from blue to red, correspond to the normalized out-of-plane displacement w/w_{max} of the plate.

C. Extension of the rationale to 2D in-plane periodicity

In this section, the extension to the case of 2D in-plane periodicity of the theoretical framework proposed in Fig. 4 is proposed. Figure 8(a) reports a schematic of the 2D mass-spring hexagonal lattice. As in the 1D case, the modulation parameter λ is here applied to the spring of stiffness k [left panel of Fig. 8(b)] or δ [left panel of Fig. 8(c)], corresponding to the springs highlighted in red. Taking the lower spring stiffness δ to 0 (we recall here that $k > \delta$) as a limiting process, two different sets of disjoint mass-spring systems are obtained [central panels of Figs. 8(b) and 8(c)]. They are characterized by a couple of natural frequencies ω with multiplicities MN or MN + 1 and MN - 1 [right panels of Figs. 8(b) and 8(c)]. As λ is varied from 0.01 to 0.1, similarly to the 1D case, the number of modes on the lower bulk band changes (or not) from MN + 1 to MN, only when the stiffer k spring is altered. This change clearly requires a spectral flow of a family of localized modes across the band gap. On the other hand, when the spring of stiffness δ is altered, the number of modes on the lower band remains MN, implying no net spectral flow.

IV. CONCLUSION AND DISCUSSION

In conclusion, we have presented a design strategy to systematically achieve localized modes in continuous elastic media based on simple selective stiffness alterations. We have demonstrated the possibility of a spectral flow across a bulk frequency gap of a family of localized modes through experimental measurements and numerical calculations in 3D structures with 1D and 2D periodicities, respectively. The underlying mechanism has been explained via a detailed analytical model. The same rationale could also be extended to three-dimensional periodicity. Although the spectral flow theorem has often been used to detect interface modes in different fields [54–56], including elasticity [57], our work has the unique feature of not requiring two distinct lattices. This allows the emergence of a localized mode at any arbitrary location within a periodic structure by solely changing a structural parameter at a single location.

We strongly believe that these results will open exciting opportunities in elastic energy localization, making it a powerful design strategy of interest in all the fields where vibrations play a crucial role, such as, for example, in resonant tracking sensors, i.e., devices that sense physical quantities based on resonance frequency shifts [58,59].

The data that support the plots within this paper and other findings of this study are available from the corresponding author upon request.

ACKNOWLEDGMENTS

M.M. is funded by the European Union's Horizon Europe programme in the framework of the ERC StG

POSEIDON under Grant Agreement No. 101039576. R.K.P. is supported by startup funds from Kansas State University and by U.S National Science Foundation Grant No. 2027455. F.A. acknowledges N. Herard, B. Skoropys, M. Coimbra, T. Lata, N. Compton, I. Frankel, and N. Boechler for an earlier investigation on the experimental realization of a mass-spring system via additive manufacturing.

All authors contributed extensively to the work presented in this paper.

The authors declare no competing financial interests.

APPENDIX A: DISPERSION BAND DIAGRAM FOR THE INFINITE STRUCTURE

Figure 9 reports the dispersion curves and mode shapes for the unit cell highlighted in yellow in Fig. 1(b) of the main text considered as infinitely repeated along the x direction. The dispersion diagram is here reported for the case of $k > \delta = k/2$. The chosen geometrical parameters are the following: (i) side of the square mass a = 10 mm, (ii) length of the beams L = 15 mm, (iii) radii of the beams corresponding to the stiffer spring are $r_1 = 1.20 \times \sqrt{2} \simeq 1.70$ mm (k) and k and k and k and k are those of the thermoplastic polymer VEROTM and are reported in the main text.

The band diagram is calculated by imposing Bloch-Floquet periodic boundary conditions over the left and right surfaces of the model and by varying the reduced wave number $k^* = k\pi/a$ along the Γ -X boundary of the first irreducible Brillouin zone ($\Gamma = 0$ and $X = \pi/a$) with a the unit cell size. Despite all the possible polarizations of the unit cell deformation (namely, bending, shear, torsional, and axial modes) reported [Fig. 9(b)], a full band gap is present (light green rectangle).

APPENDIX B: PHOTOGRAPH OF THE MANUFACTURED SAMPLES

Twenty specimens are fabricated. Figure 10 shows a photograph of the two sets of manufactured samples: those exhibiting $k < \delta$ (top part of the photograph) and those with $k > \delta$ (bottom part of the photograph). The stiffness modulation in both cases only concerns the central spring.

APPENDIX C: EXPERIMENTAL MEASUREMENTS

Figure 11(a) reports a schematic representation of the experimental configurations adopted to measure the frequency response functions presented in Figs. 1(c) and 2(b) and to reconstruct the mode shapes reported in Fig. 3 of the main text. In the first case (transmissibility configuration), the excitation F(t) (red arrow) was provided at one edge of the samples (mass #14), and the responses collected

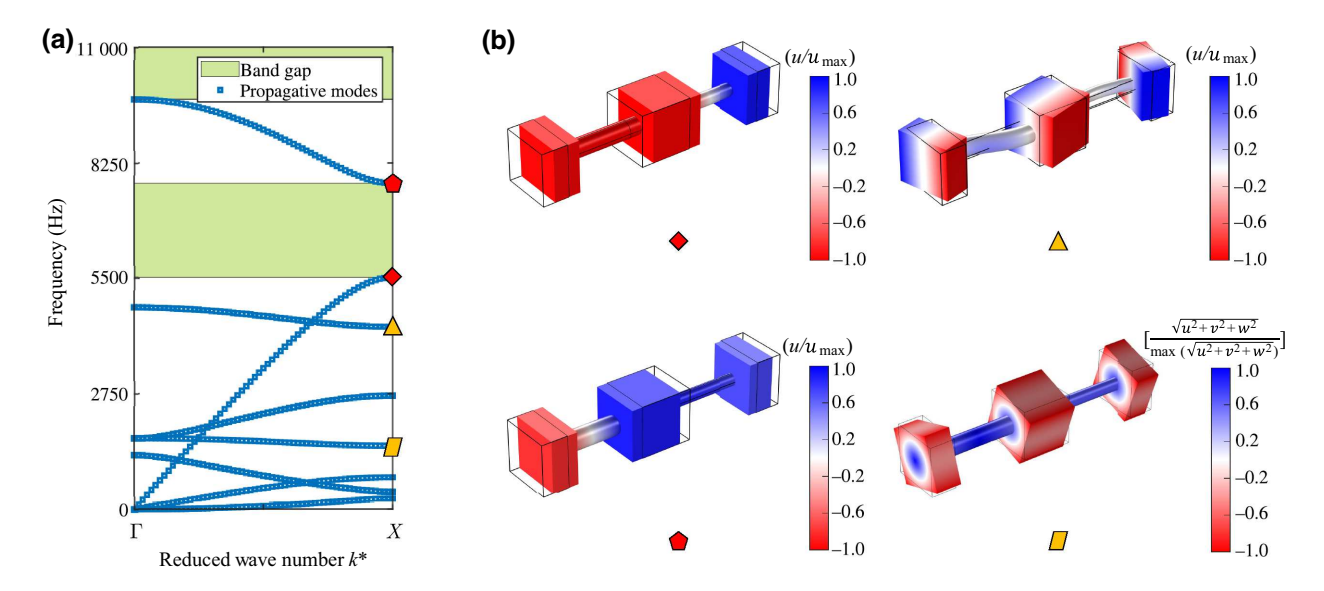


FIG. 9. Dispersion diagram and mode shapes of the continuous unit cell. (a) Dispersion diagram of the continuous unit cell reported in Fig. 1(b) of the main text in the 0–11-kHz frequency range. A full frequency band gap is clearly visible and highlighted as the light green rectangle. (b) Mode shapes corresponding to the red and yellow markers in (a) showing different types of mode polarization. The first two masses of the lowest longitudinal mode have the same phase, but are in opposition to the third one. On the contrary, in the higher longitudinal mode at the same wave number π/a , the second and third masses are in phase and in opposition to the first one.

at the opposite edge (mass #1)—light blue star and circle markers with red contours. The frequency response functions were calculated as the ratio of the detected (averaged over 100 times) and the imparted velocities at the acquisition and excitation points, respectively. Two lasers were

used to measure the axial velocity of the masses: the OFV 353, collecting the signal at the excited point (reference measurement), and the PSV 400, measuring the velocity amplitude in the selected masses of the chains (points of measurements). The sensitivity of the lasers was set to

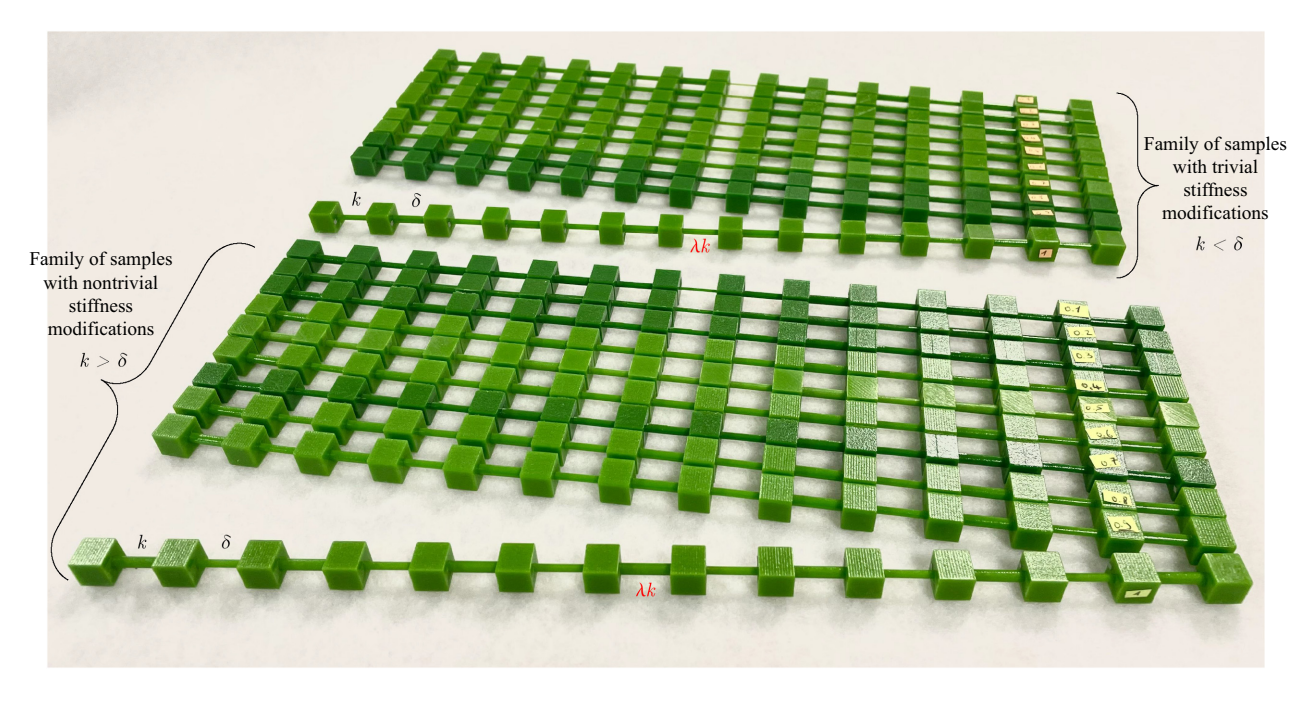


FIG. 10. Photograph of the manufactured samples. The two sets of manufactured samples are divided into those exhibiting $k < \delta$ (top part of the photograph) and those with $k > \delta$ (bottom part of the photograph).

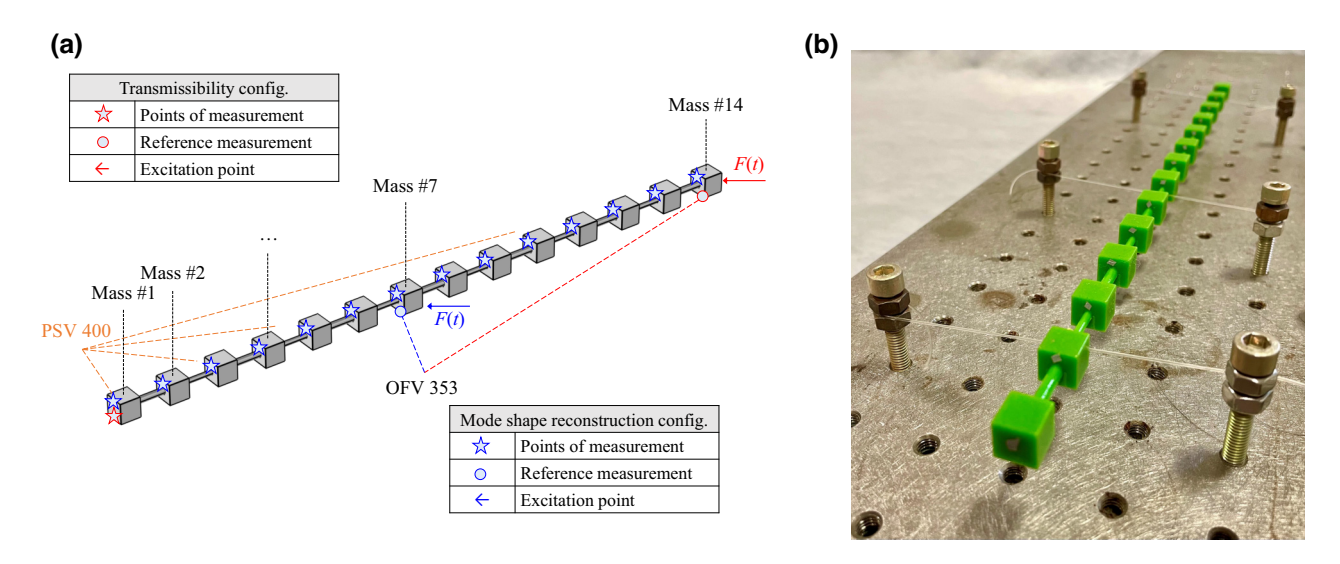


FIG. 11. Schematic representation of the experimental configurations. (a) The red and blue arrows point at the masses where the excitation was provided: at the edge (mass #14) and the center (mass #7) of the chains, respectively. This allowed us to conduct the measurements in two experimental setups. (i) The *transmissibility configuration*, where the excitation was provided at one edge of the samples (mass #14) and data collected at the other edge (mass #1). This configuration has been adopted to measure the frequency response functions shown in Figs. 1(c) and 2(b) of the main text. (ii) The *mode shape reconstruction configuration*, where the excitation was provided at the center of the chain (mass #7) and data collected at all the masses of samples #1–#14. This configuration allowed us to reconstruct the mode shapes reported in Fig. 3 of the main text. Two lasers, the PDV 100 and PSV 400, were used to measure the axial velocity at the excitation points and at the masses composing the chains. The stars indicate the scanning points of measurement on the structures, while the circles indicate the acquisition points used for reference. The reference measurements (blue and red lines) taken at the excited masses are used to determine the input velocity with respect to which the results have been normalized. The numerical models used to calculate the transmission spectra reported in Fig. 17 below reflect the first configuration (excitation at one edge). (b) Photograph of the experimental configuration used to reproduce the free-free boundary conditions for the specimens under investigation.

 $20 \,(\text{mm/s})/\text{V}$. The data measurements corresponding to each λ have been individually normalized with respect to their maximum value.

A similar procedure was adopted for the experimental mode shape reconstruction configuration reported in Fig. 3 of the main text, but mass #7 was selected as the excitation point (blue arrow) and the acquisition of data was performed on all the masses (#1—#14)—light blue star and circle markers with blue contours.

The structures were put in suspension by thin ropes [Fig. 11(b)], so as to reproduce free boundary conditions. Impulsive excitation was provided by manually hitting the masses through a 3-mm hexagonal key. We calibrated the procedure so that energy of approximately up to 10 kHz was injected into the specimen, which provided a sufficient broadband excitation with respect to the localized mode to observe. The rigid longitudinal translation modes at zero frequency are filtered out in the experimental measurements through a high-pass band filter.

APPENDIX D: DISCRETE MODELS

In this appendix, we show, through a discrete model, how a localized mode can be induced anywhere in an otherwise homogeneous finite mass-spring chain by simply varying the stiffness of a single spring.

1. Localized modes when $0 < \lambda < 1$

Figure 12 reports a mass-spring discrete system with identical masses m (green dots) and alternating springs of stiffness k and δ . The finite chain exhibits 2N masses, where N is the number of unit cells (blue dashed rectangle). Free boundary conditions apply at its edges.

The governing equations are thus given by

$$m\ddot{u}_r + k_r(u_r - u_{r-1}) + k_{r+1}(u_r - u_{r+1}) = 0,$$

 $r = 1, 2, \dots, 2N.$ (D1)

The stiffness of the springs is assumed to be $k_r = k$ for odd values of r and $k_r = \delta$ for even values of r. To satisfy the free boundary conditions, $k_1 = k_{2N+1} = 0$ applies. In addition, the stiffness of an arbitrary spring (highlighted in red) is set to λk , where λ takes values in the [0, 1] range.

For the sake of brevity, the analysis and results are here presented only for the case of N being odd—the cases of an even number of unit cells N and of an odd number of masses, 2N + 1, can be derived by similar arguments and

FIG. 12. Schematic representation of the mass-spring chain with an interface. A mass-spring finite discrete system with identical masses m and alternating springs of stiffness k and δ is presented. The chain is composed of N unit cells (blue dashed rectangle) and 2N masses and springs. The spring stiffness is $k_r = k$ for odd values of r and $k_r = \delta$ for even values of r. Free boundary conditions apply at its edges. The interface spring stiffness (in red) is modified by a factor λ .

are briefly discussed at the end of this section. Two distinct cases are examined: $k > \delta$ and $k < \delta$ (in both cases, the mass is set to m = 1).

Figure 13(a) reports the natural frequencies for a finite chain characterized by N=40, k=2 and $\delta=1$, while Fig. 13(b) corresponds to the case of k=1 and $\delta=2$. As expected, a band gap in the natural frequencies due to the dimer chain is present and it spans the frequency range $\omega_1 = \sqrt{2\delta/m}$ to $\omega_2 = \sqrt{2k/m}$. The key point to note here is that the dispersion curves have a band gap when $k \neq \delta$ and the band gap closes when $k=\delta$.

As λ varies in the range [0, 1], the natural frequencies of the two chains show distinct behaviors. Most of the natural frequencies are restricted to lie in the two dispersion bulk bands. In the case of $k > \delta$ [Fig. 13(a)], a spectral flow of a single mode happens from the bottom to the top band as λ increases. In contrast, no such spectral flow is observed in the case of $k < \delta$ [Fig. 13(b)].

Figure 14 reports the mode shapes of the (N+1)th mode for two distinct λ values. In Figs. 14(a) and 14(b) the mode shapes for both the chains at $\lambda=1$ are reported. It is worth noting that all the modes of a finite chain with free ends and $\lambda=1$ lie in the dispersion pass bands. In addition, they can be identified with zero wave-number Bloch modes of a large supercell (shown in the next subsection). Hence, they are bulk modes and their deformation involves the entire chain. Figures 14(c) and 14(d) report the mode shapes for these chains when $\lambda=0.5$. The chain with $k>\delta$ has a mode clearly localized at the interface [Fig. 14(c)] and its displacement magnitude drops rapidly away from the interface. In contrast, the same mode for the chain with $k<\delta$ is characterized by a mode

involving the displacement of all the masses of the chain [Fig. 14(d)].

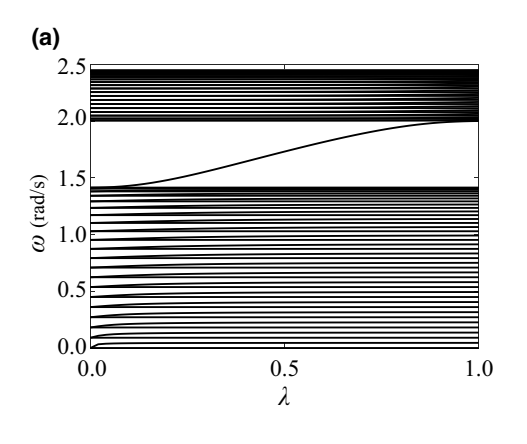
2. Mathematical explanation of why the modes of the finite chains considered at $\lambda = 0$ and $\lambda = 1$ all have frequencies in the bulk spectrum of an infinite chain

Here we show that the modes of the finite chains considered at $\lambda=0$ and $\lambda=1$ all have frequencies in the bulk spectrum of an infinite chain. In other words, they lie in the dispersion pass bands. This observation provides the foundation to establish spectral flow as λ varies from 0 to 1. For $\lambda=0$ or $\lambda=1$, the ends are free and the stiffness of the springs alternates between k and δ . Two possibilities thus arise, as illustrated in Fig. 15, depending on whether the total number of masses is even or odd.

a. Case 1: chain with 2N masses

The case of a chain having an even number of masses, as that reported in Fig. 15(a), is considered first. The origin is fixed at the left end side of the chain and the distance between adjacent masses is set to be unity. The governing equation may be written in matrix form as $\mathbf{M}\ddot{\mathbf{u}} + \mathbf{K}\mathbf{u} = \mathbf{0}$. To determine the natural frequencies and mode shapes, we set $\mathbf{u}(t) = e^{i\omega t}\mathbf{U}$ and the governing equation becomes $\mathbf{K}\mathbf{U} = \omega^2\mathbf{M}\mathbf{U}$. The mode shapes \mathbf{U} and the natural frequencies ω are thus obtained from the eigenvalue problem

$$\mathbf{D}\mathbf{U} = \omega^2 \mathbf{U}.\tag{D2}$$



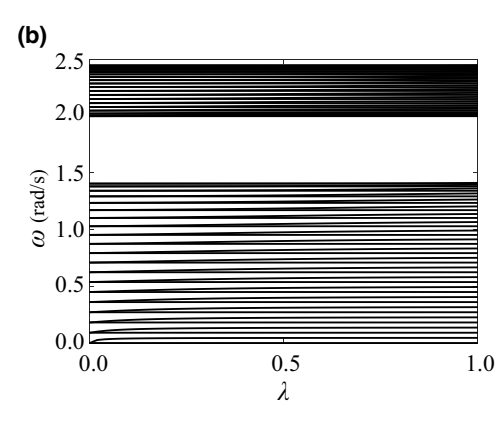
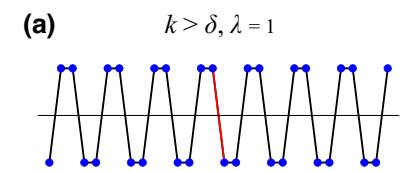
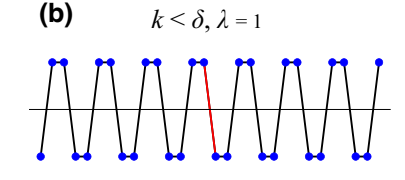
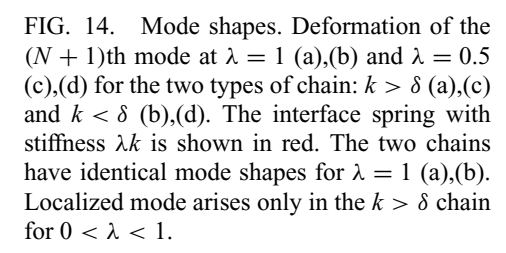
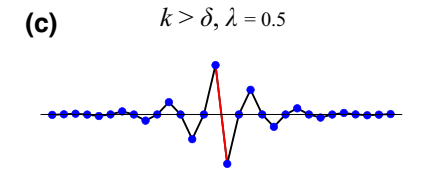


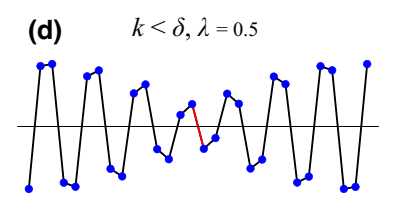
FIG. 13. Analytical eigenfrequencies. Natural frequencies for the chain with N=40 and (a) k=2, $\delta=1$ and (b) k=1, $\delta=2$. The frequency of a mode traverses the band gap as λ varies from 0 to 1 in the chain with $k>\delta$ only.











Here $\mathbf{D} = \mathbf{M}^{-1}\mathbf{K}$ is the dynamic matrix. Since the chain has reflection symmetry about its center x = N + 1/2, the dynamic matrix \mathbf{D} commutes with its corresponding reflection operator \mathbf{R} . In particular, \mathbf{D} commutes with the operator whose components are

$$R_{ij} = \begin{cases} 1 & \text{if } j = i + 2N - 1, \\ 0 & \text{otherwise.} \end{cases}$$

Physically, this commutation means that **D** remains identical when the coordinate axis is reflected about the center of the chain. The mode shapes of **D** are thus eigenvectors of **R** [60]. Hence, each mode shape can be identified with a corresponding eigenvalues of **R**, namely, $\{-1, +1\}$. Physically, they correspond to even $\lambda_R = 1$ and odd $\lambda_R = +1$ mode shapes about the center, respectively.

Each of these mode shapes can be identified with a Bloch mode of a large supercell. First, let us consider an even mode shape with components $U = \{U_p, p = 1, 2, ..., 2N\}$. These components satisfy the relation

$$U_p = U_{2N+1-p}, \qquad p = 1, 2, \dots, 2N.$$
 (D3)

Let us now consider the displacement vector **w** of an infinite chain with components w_r , $r \in \mathbb{Z}$:

$$w_r = U_p, \qquad r = p \mod (2N).$$
 (D4)

By direct substitution into the governing equations, and noting that $U_1 = U_{2N}$ and thus $w_1 = w_{2N} = w_{2N+1}$, it can

be verified that $e^{i\omega t}$ **w** satisfies the governing equations of an infinite chain. Thus, **w** is the mode shape of an infinite chain and it satisfies the relation

$$w_{r+2N} = w_r, \qquad r \in \mathbb{Z}.$$
 (D5)

Finally, let us show that the frequency ω of this mode lies in the bulk dispersion band. To this end, we consider a supercell of N unit cells having 2N masses. The mode shape corresponding to a Bloch mode $\mathbf{b} = (b_1, b_2, \dots, b_{2N})$ of this supercell at wave number $\mu = 0$ satisfies

$$b_{r+2N} = b_r, \qquad r \in \mathbb{Z}.$$
 (D6)

Comparing the above condition with Eq. (D5), and noting that **b** and **w** satisfy the same governing equations, we infer that **w** is a Bloch mode of the supercell at wave number $\mu = 0$. Noting that the pass band of the dispersion surface is the same for the supercell and the unit cell, we conclude that the frequency ω lies in the pass band of the dispersion surface.

Next, let us show that the frequency of an odd mode shape also lies in the pass bands of the dispersion surface. Again, let its components be $\mathbf{U} = (U_1, U_2, \dots, U_{2N})$, satisfying

$$U_p = -U_{2N+1-p}, p = 1, 2, \dots, 2N.$$
 (D7)

Let us consider the displacement of a finite chain with 4N masses and having components $V = (V_1, V_2, ..., V_{4N})$

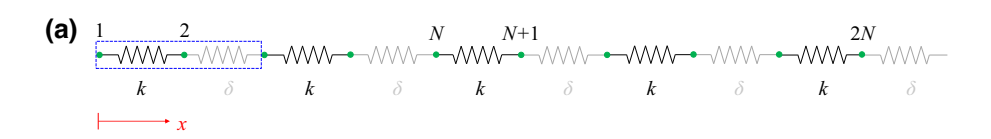
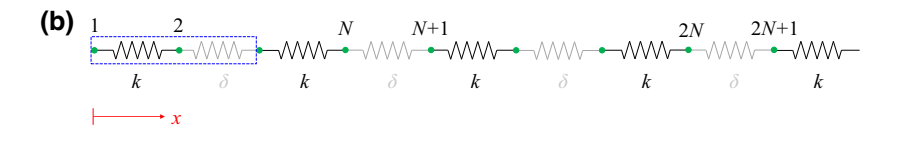


FIG. 15. Possible configurations of the mass-spring chain. Two possible finite configurations with (a) even and (b) odd numbers of masses are possible. The distance between two adjacent masses is set to 1.



given by

$$V_r = \begin{cases} U_r, & r \le 2N, \\ U_{4N+1-r}, & 2N < r \le 4N. \end{cases}$$
 (D8)

This longer chain has free boundary conditions at both ends. Let us discuss why the components of V represent a mode shape of the chain with 4N masses at the same frequency as the odd mode shape of the shorter chain with 2N masses. A direct check shows that the components of V satisfy the governing equations at masses r = 2N and r = 2N + 1. At all other masses, the governing equation is satisfied as a consequence of being an odd mode shape of the shorter chain with 2N masses.

From Eq. (D8), we have the following relation between the components of V:

$$V_r = U_r = U_{4N+1-(4N+1-r)} = V_{4N+1-r}$$

for all $1 \le r \le 2N$. (D9)

Thus, the displacement vector \mathbf{V} is an even mode shape of a chain about x = 2N + 1/2. We have shown above that this mode can be identified with a unique mode of the infinite chain, or, equivalently, a zero wave-number Bloch mode of a supercell, here of length 4N.

b. Case 2: chain with 2N + 1 masses

Finally, let us analyze the chain with an odd number of masses, shown in Fig. 15(b). Let us consider a mode shape with displacement components $\mathbf{U} = (U_1, U_2, \dots, U_{2N+1})$ and frequency ω . Note that this mode shape can be neither odd nor even, since the chain does not have reflection symmetry about its center. Again, let us consider the displacement vector of a chain with 4N+2 masses having components $\mathbf{V} = (V_1, V_2, \dots, V_{4N+2})$. These components are given by

$$V_r = \begin{cases} U_r, & r \le 2N+1, \\ U_{4N+3-r}, & r > 2N+1. \end{cases}$$
 (D10)

A direct check shows that V_r satisfies the governing equations at masses r=2N+1 and 2N+2. At all other masses, it is satisfied as a consequence of being a mode shape of the shorter chain of 2N+1 masses. Thus, **V** is a mode shape of the longer chain with the same frequency ω . Using a reasoning similar to Eq. (D9), we see that V_r is an even mode shape of a chain of length 4N+2, centered about x=2N+3/2. We have shown above that such an even mode in a chain with an even number of masses (4N+2 here) can be identified with a unique mode of the infinite chain, or, equivalently, a zero wave-number Bloch mode of a supercell with 4N+2 masses. Thus, all the modes of a finite chain lie in the dispersion pass bands.

3. Localized modes when $\lambda > 1$

Figure 16 presents the natural frequencies for both $k > \delta$ (left panel) and $k < \delta$ (right panel) when $\lambda > 1$.

In the first scenario $(k > \delta)$, a localized mode may still appear in the band gap, depending on the relative values of k and δ . However, this mode is trivial in the sense that it is not guaranteed to span the band gap as parameter λ is varied. This means that, when $\lambda > 1$, the localization depends on the specific material and geometric properties, with the spectral-flow based arguments described above no longer guaranteeing the localization of the mode in the band gap. No localized mode appears when $\lambda > 1$ (right panel).

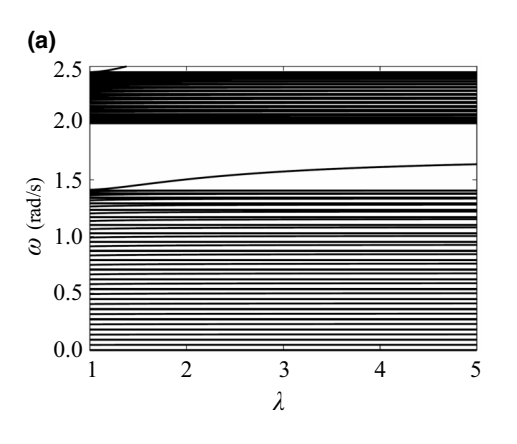
APPENDIX E: ADDITIONAL NUMERICAL AND ANALYTICAL COMPARISONS OF THE SPECTRAL FLOW

In this appendix, a time domain numerical simulation is performed by solving the following set of differential equations of motion for a discrete system of masses and springs through an in-house developed code including a Maxwell dissipation model by using a fourth-order Runge-Kutta method:

$$m\ddot{u}_r = k_r(u_{r-1} - u_r) - k_{r+1}(u_r - u_{r+1}) - \frac{m}{\tau}\dot{u}_r.$$
 (E1)

Here r = 1, 2, ..., 2N (with 2N the total number of the masses composing the chains), m is the mass of the particles, and $k_r = EA_r/L$ is the longitudinal beam stiffness linking the masses, where E, A_r , and L are Young's modulus, the beam cross-section area, and the beam length, respectively. The double- and single-dot notation represent the second and first time derivatives, respectively. Freefree boundary conditions for the first and last particles are considered such that $k_1 = 0$ (or, equivalently, $u_0 = u_1$) and $k_{2N+1} = 0$ (or, equivalently, $u_{2N+1} = u_{2N}$). Elastic waves are generated by imposing an initial velocity condition on the first particle to mimic the experimental kick [namely, $\dot{u}_1(t=0) = 5e^{-3} \text{ m s}^{-1}$]. The system of equations is linear; thus, the amplitude of the initial condition can be arbitrarily taken. To account for wave attenuation, a linear viscous on-site dissipation model is used, with a time of decay $\tau = 0.8$ ms (this time of decay has been fitted from the experimental measurements).

Figure 17 reports the frequency response functions in the 0–11-kHz frequency range for the two study cases $[k > \delta]$ in Fig. 17(a) and $k < \delta$ in Fig. 17(b)] when ten different values of λ are adopted. In the first case, the spectral flow of the eighth mode from the lower to the upper bulk region is clearly observed as energy spots passing across the entire band gap when λ is varied in the [0.1, 1] range. On the contrary, when $k < \delta$, no crossing is observed as parameter λ is changed. In both cases, excellent agreement between the numerical simulations and the analytically calculated mode shapes is found. In these calculations, contrary to



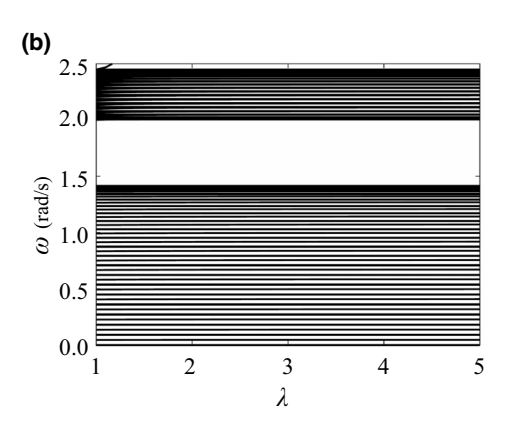


FIG. 16. Natural frequencies when $\lambda > 1$. A localized mode appears in the chain characterized by $k > \delta$ (a), but without spanning the whole band gap. No localized mode appears when $\lambda > 1$ (b).

the measurements [Fig. 1(c) of the main text], no high-pass filters are applied.

APPENDIX F: MECHANICAL AND GEOMETRICAL PROPERTIES FOR THE NUMERICAL MODELS

Numerical simulations are conducted via the finite-element software COMSOL Multiphysics® for both the (i) 1D mass-spring systems and (ii) 2D hexagonal lattice. In both cases, domains are meshed by means of three-dimensional tetrahedral elements of maximum size $L_{\rm FE}=$

 $\bar{\lambda}_{min}/10$, which is found to provide accurate eigensolutions up to the frequency of interest (with $\bar{\lambda}_{min}$ the smallest wavelength of interest). Quadratic elements have been used to accurately capture the flexural deformation since the strain is not constant but varies linearly across the cross section. In both cases, linear elastic constitutive laws are assumed for the materials.

APPENDIX G: HEXAGONAL LATTICE DISCRETE MODEL

In this appendix, we present the details of how the discrete model (made of masses and springs) has guided the

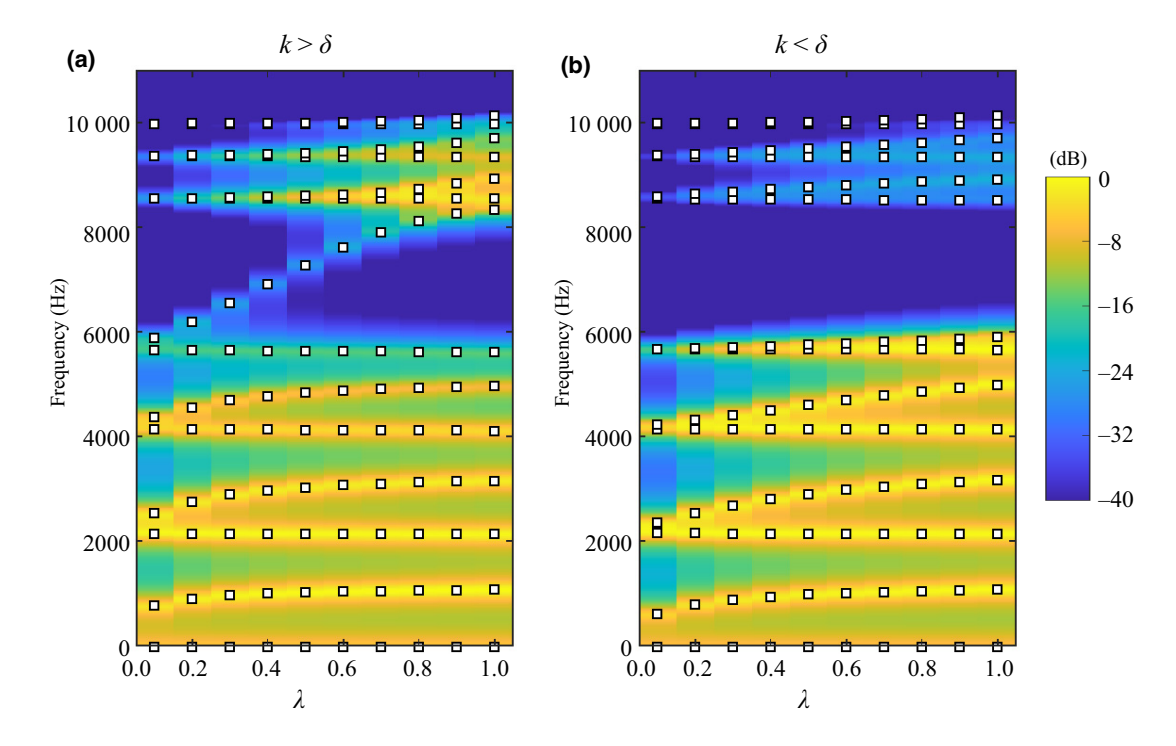
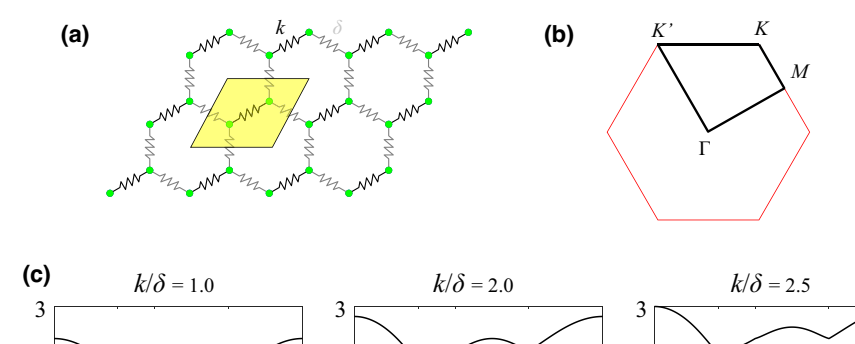
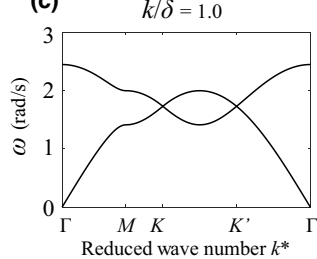
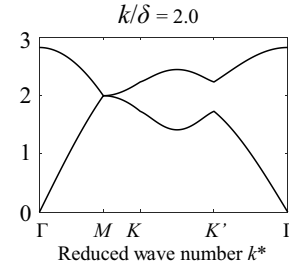


FIG. 17. Numerical calculations versus the analytical model. Numerical frequency response functions (color map) in the 0–11-kHz frequency range for the two classes of elastic chain: (a) $k > \delta$ and (b) $k < \delta$ for different values of λ . In the first case, the spectral flow of the eighth mode from the lower to the upper bulk band is clearly observed (the mode passes across the entire band gap as λ is varied in the [0.1, 1] range). On the contrary, in the latter case, no crossing is observed. Overlaid square white dots indicate the analytically calculated eigenmodes.







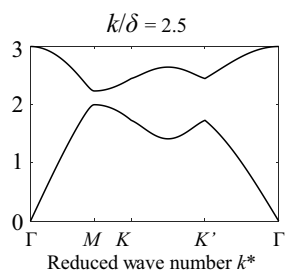


FIG. 18. Dispersion curves for the discrete hexagonal lattice for different ratios of k and δ . (a) Discrete model consisting of point masses at the vertices of a hexagonal lattice (green dots) connected by linear springs of stiffness k or δ (in black and gray, respectively). The light yellow parallelogram indicates the unit cell. (b) The first irreducible Brillouin zone (black line) corresponding to the unit cell reported in (a). (c) Dispersion curves for different ratios of k and δ . For a given value of 1 kg/m³ for the masses, no band gap (left panel) is found when $k/\delta = 1$, whereas a band gap (right panel) is opened when $k/\delta > 2$.

design of the unit cells of the continuous elastic system hosting the spectral flow of a family of localized modes. The discrete model is shown in Fig. 18(a) and consists of point masses at the vertices of a hexagonal lattice (green dots) connected by linear springs of stiffness k or δ (highlighted in black and gray, respectively). The lattice vectors are $\mathbf{a}_1 = a[1, 0]$ and $\mathbf{a}_2 = a[\cos \pi/3, \sin \pi/3]$. Each mass has one degree of freedom and can only move out of plane. The light yellow parallelogram indicates the unit cell. It has $C_{2\nu}$ symmetry since there are two springs of distinct stiffness (k and δ). Hence, its first irreducible Brillouin zone [Fig. 18(b)] is the quadrilateral Γ -M-K-K', as shown by the black lines. Its coordinates are $M = (1, 1/\sqrt{3})\pi/a$, $K = (2/3, 2/\sqrt{3})\pi/a$, K' = $(-2/3, 2/\sqrt{3})\pi/a$, and $\Gamma = (0, 0)$, with a the size of the unit cell.

For a given value of the masses (in this case fixed to 1 kg/m^3 for the sake of simplicity), we can show that properly choosing the ratio of the springs k and δ , we can open a band gap when $k > 2\delta$ [see Fig. 18(c)]. Based on these results, an elastic analogue comprising the beam segments in a hexagonal lattice configuration is considered. A shorter (longer) beam segment corresponds to a higher (lower) flexural stiffness.

- [1] M. Z. Hasan and C. L. Kane, Colloquium: Topological insulators, Rev. Mod. Phys. **82**, 3045 (2010).
- [2] A. Souslov, B. C. Van Zuiden, D. Bartolo, and V. Vitelli, Topological sound in active-liquid metamaterials, Nat. Phys. 13, 1091 (2017).
- [3] N. Stenger, M. Wilhelm, and M. Wegener, Experiments on elastic cloaking in thin plates, Phys. Rev. Lett. 108, 014301 (2012).
- [4] Y. Chen, B. Wu, Y. Su, and W. Chen, Tunable two-way unidirectional acoustic diodes: Design and simulation, J. Appl. Mech. 86, 031010 (2019).

- [5] Y. Chen, Y. Huang, C. Lü, and W. Chen, A two-way unidirectional narrow-band acoustic filter realized by a graded phononic crystal, J. Appl. Mech. 84, 091003 (2017).
- [6] S. Stützer, Y. Plotnik, Y. Lumer, P. Titum, N. H. Lindner, M. Segev, M. C. Rechtsman, and A. Szameit, Photonic topological Anderson insulators, Nature 560, 461 (2018).
- [7] K. Aouali, N. Kacem, N. Bouhaddi, E. Mrabet, and M. Haddar, Efficient broadband vibration energy harvesting based on tuned non-linearity and energy localization, Smart Mater. Struct. 29, 10LT01 (2020).
- [8] Y. Pennec, J. O. Vasseur, B. Djafari-Rouhani, L. Dobrzyński, and P. A. Deymier, Two-dimensional phononic crystals: Examples and applications, Surf. Sci. Rep. 65, 229 (2010).
- [9] R. V. Craster and J. Kaplunov, *Dynamic Localization Phenomena in Elasticity, Acoustics and Electromagnetism* (Springer, Springer Vienna, 2013), Vol. 547.
- [10] A. Lagendijk, B. Van Tiggelen, and D. S. Wiersma, Fifty years of Anderson localization, Phys. Today 62, 24 (2009).
- [11] P. Sheng, Scattering and Localization of Classical Waves in Random Media (World Scientific, Singapore, 1990), Vol. 8.
- [12] R. L. Weaver, Anderson localization of ultrasound, Wave Motion 12, 129 (1990).
- [13] L. Ye, G. Cody, M. Zhou, P. Sheng, and A. N. Norris, Observation of bending wave localization and quasi mobility edge in two dimensions, Phys. Rev. Lett. 69, 3080 (1992).
- [14] H. Hu, A. Strybulevych, J. Page, S. E. Skipetrov, and B. A. van Tiggelen, Localization of ultrasound in a three-dimensional elastic network, Nat. Phys. 4, 945 (2008).
- [15] M. Zhang, W. Zhong, and X. Zhang, Defect-free localized modes and coupled-resonator acoustic waveguides constructed in two-dimensional phononic quasicrystals, J. Appl. Phys. 111, 104314 (2012).
- [16] A. Hladky-Hennion, J. Vasseur, S. Degraeve, C. Granger, and M. De Billy, Acoustic wave localization in onedimensional Fibonacci phononic structures with mirror symmetry, J. Appl. Phys. 113, 154901 (2013).
- [17] X. Chen, A. Weathers, J. Carrete, S. Mukhopadhyay, O. Delaire, D. A. Stewart, N. Mingo, S. N. Girard, J. Ma, and

- D. L. Abernathy, *et al.*, Twisting phonons in complex crystals with quasi-one-dimensional substructures, Nat. Commun. **6**, 1 (2015).
- [18] T. Požar, J. Laloš, A. Babnik, R. Petkovšek, M. Bethune-Waddell, K. J. Chau, G. V. Lukasievicz, and N. G. Astrath, Isolated detection of elastic waves driven by the momentum of light, Nat. Commun. 9, 3340 (2018).
- [19] A. Khelif, A. Choujaa, B. Djafari-Rouhani, M. Wilm, S. Ballandras, and V. Laude, Trapping and guiding of acoustic waves by defect modes in a full-band-gap ultrasonic crystal, Phys. Rev. B 68, 214301 (2003).
- [20] S. Benchabane, A. Khelif, A. Choujaa, B. Djafari-Rouhani, and V. Laude, Interaction of waveguide and localized modes in a phononic crystal, EPL (Europhys. Lett.) 71, 570 (2005).
- [21] Z.-Z. Yan, C. Zhang, and Y.-S. Wang, Analysis of wave propagation and localization in periodic/disordered layered composite structures by a mass-spring model, Appl. Phys. Lett. 94, 161909 (2009).
- [22] L.-Y. Zheng, F. Allein, V. Tournat, V. Gusev, and G. Theocharis, Granular graphene: Direct observation of edge states on zigzag and armchair boundaries, Phys. Rev. B 99, 184113 (2019).
- [23] K. F. Graff, Wave Motion in Elastic Solids (Courier Corporation, 2012).
- [24] R. Marchal, O. Boyko, B. Bonello, J. Zhao, L. Belliard, M. Oudich, Y. Pennec, and B. Djafari-Rouhani, Dynamics of confined cavity modes in a phononic crystal slab investigated by in situ time-resolved experiments, Phys. Rev. B 86, 224302 (2012).
- [25] A. Yang, P. Li, Y. Wen, C. Yang, D. Wang, F. Zhang, and J. Zhang, High-Q cross-plate phononic crystal resonator for enhanced acoustic wave localization and energy harvesting, Appl. Phys. Express 8, 057101 (2015).
- [26] S.-H. Jo, H. Yoon, Y. C. Shin, and B. D. Youn, A graded phononic crystal with decoupled double defects for broadband energy localization, Int. J. Mech. Sci. **183**, 105833 (2020).
- [27] S.-H. Jo, H. Yoon, Y. C. Shin, W. Choi, C.-S. Park, M. Kim, and B. D. Youn, Designing a phononic crystal with a defect for energy localization and harvesting: Supercell size and defect location, Int. J. Mech. Sci. 179, 105670 (2020).
- [28] M. Sigalas, Defect states of acoustic waves in a twodimensional lattice of solid cylinders, J. Appl. Phys. 84, 3026 (1998).
- [29] S. Benchabane, O. Gaiffe, R. Salut, G. Ulliac, V. Laude, and K. Kokkonen, Guidance of surface waves in a micron-scale phononic crystal line-defect waveguide, Appl. Phys. Lett. 106, 081903 (2015).
- [30] Y.-F. Wang, T.-T. Wang, J.-P. Liu, Y.-S. Wang, and V. Laude, Guiding and splitting Lamb waves in coupled-resonator elastic waveguides, Compos. Struct. **206**, 588 (2018).
- [31] E. Prodan and C. Prodan, Topological phonon modes and their role in dynamic instability of microtubules, Phys. Rev. Lett. **103**, 248101 (2009).
- [32] R. Süsstrunk and S. D. Huber, Observation of phononic helical edge states in a mechanical topological insulator, Science 349, 47 (2015).

- [33] L. M. Nash, D. Kleckner, A. Read, V. Vitelli, A. M. Turner, and W. T. Irvine, Topological mechanics of gyroscopic metamaterials, Proc. Natl. Acad. Sci. 112, 14495 (2015).
- [34] C. He, X. Ni, H. Ge, X.-C. Sun, Y.-B. Chen, M.-H. Lu, X.-P. Liu, and Y.-F. Chen, Acoustic topological insulator and robust one-way sound transport, Nat. Phys. **12**, 1124 (2016).
- [35] S. H. Mousavi, A. B. Khanikaev, and Z. Wang, Topologically protected elastic waves in phononic metamaterials, Nat. Commun. 6, 1 (2015).
- [36] M. Miniaci, R. Pal, B. Morvan, and M. Ruzzene, Experimental observation of topologically protected helical edge modes in patterned elastic plates, Phys. Rev. X 8, 031074 (2018).
- [37] X. Zhang, M. Xiao, Y. Cheng, M.-H. Lu, and J. Christensen, Topological sound, Commun. Phys. 1, 1 (2018).
- [38] A. Darabi, M. Collet, and M. J. Leamy, Experimental realization of a reconfigurable electroacoustic topological insulator, Proc. Natl. Acad. Sci. 117, 16138 (2020).
- [39] Z.-G. Chen, W. Zhu, Y. Tan, L. Wang, and G. Ma, Acoustic realization of a four-dimensional higher-order Chern insulator and boundary-modes engineering, Phys. Rev. X 11, 011016 (2021).
- [40] G. Ma, M. Xiao, and C. T. Chan, Topological phases in acoustic and mechanical systems, Nat. Rev. Phys. 1, 281 (2019).
- [41] M. Miniaci and R. Pal, Design of topological elastic waveguides, J. Appl. Phys. 130, 141101 (2021).
- [42] H. C. Po, H. Watanabe, and A. Vishwanath, Fragile topology and Wannier obstructions, Phys. Rev. Lett. 121, 126402 (2018).
- [43] V. Peri, Z.-D. Song, M. Serra-Garcia, P. Engeler, R. Queiroz, X. Huang, W. Deng, Z. Liu, B. A. Bernevig, and S. D. Huber, Experimental characterization of fragile topology in an acoustic metamaterial, Science 367, 797 (2020).
- [44] Z.-D. Song, L. Elcoro, and B. A. Bernevig, Twisted bulk-boundary correspondence of fragile topology, Science 367, 794 (2020).
- [45] H. Watanabe and H. C. Po, Fractional corner charge of sodium chloride, Phys. Rev. X 11, 041064 (2021).
- [46] K. Chen, M. Weiner, M. Li, X. Ni, A. Alù, and A. B. Khanikaev, Nonlocal topological insulators: Deterministic aperiodic arrays supporting localized topological states protected by nonlocal symmetries, Proc. Natl. Acad. Sci. 118, e2100691118 (2021).
- [47] W. A. Benalcazar, T. Li, and T. L. Hughes, Quantization of fractional corner charge in *C*_n-symmetric higher-order topological crystalline insulators, Phys. Rev. B **99**, 245151 (2019).
- [48] C. W. Peterson, T. Li, W. Jiang, T. L. Hughes, and G. Bahl, Trapped fractional charges at bulk defects in topological insulators, Nature **589**, 376 (2021).
- [49] Y. Huang, Y. Huang, W. Chen, and R. Bao, Flexible manipulation of topologically protected waves in onedimensional soft periodic plates, Int. J. Mech. Sci. 170, 105348 (2020).

- [50] H. Wang, D. Liu, W. Fang, S. Lin, Y. Liu, and Y. Liang, Tunable topological interface states in one-dimensional extended granular crystals, Int. J. Mech. Sci. 176, 105549 (2020).
- [51] M. Cajić, J. Christensen, and S. Adhikari, Tuning of topological interface modes in an elastic beam array system with inerters, Int. J. Mech. Sci. 205, 106573 (2021).
- [52] J. Köpfler, T. Frenzel, M. Kadic, J. Schmalian, and M. Wegener, Topologically protected twist edge states for a resonant mechanical laser-beam scanner, Phys. Rev. Appl. 11, 034059 (2019).
- [53] M. Miniaci, A. S. Gliozzi, B. Morvan, A. Krushynska, F. Bosia, M. Scalerandi, and N. M. Pugno, Proof of concept for an ultrasensitive technique to detect and localize sources of elastic nonlinearity using phononic crystals, Phys. Rev. Lett. 118, 214301 (2017).
- [54] T. L. Hughes, E. Prodan, and B. A. Bernevig, Inversion-symmetric topological insulators, Phys. Rev. B **83**, 245132 (2011).

- [55] J.-B. Touchais, P. Simon, and A. Mesaros, Robust propagating in-gap modes due to spin-orbit domain walls in graphene, Phys. Rev. B 106, 035139 (2022).
- [56] S. Ryu, C. Mudry, H. Obuse, and A. Furusaki, Z₂ topological term, the global anomaly, and the two-dimensional symplectic symmetry class of Anderson localization, Phys. Rev. Lett. 99, 116601 (2007).
- [57] M. Ruzzene, E. Prodan, and C. Prodan, Dynamics of elastic hyperbolic lattices, Extreme Mech. Lett. **49**, 101491 (2021).
- [58] C. T.-C. Nguyen, Mems technology for timing and frequency control, IEEE Trans. Ultrason. Ferroelectr. Freq. Control 54, 251 (2007).
- [59] J. Van Beek and R. Puers, A review of MEMS oscillators for frequency reference and timing applications, J. Micromech. Microeng. 22, 013001 (2011).
- [60] M. S. Dresselhaus, G. Dresselhaus, and A. Jorio, *Group Theory: Application to the Physics of Condensed Matter* (Springer Science & Business Media, Springer Berlin, Heidelberg, 2007).